Revista Mexicana de Astronomía y Astrofísica, 61, 240-260, (2025)

OPEN ACCESS https://doi.org/10.22201/ia.01851101p.2025.61.03.12

RMxAA REVISTA MEXICANA DE ASTRONOMÍA Y ASTROFÍSICA

Characterization and First Analysis of Three Shallow-Contact Binary Systems

C. Barani[1], **R. Michel**[2], **F. Acerbi**[3] **and P. Santillán-Ortega**[4]

[1] *Independent Researcher - Via Verdi 25, 26845 Codogno (LO), Italy.*
[2] *Universidad Nacional Autónoma de México, Instituto de Astronomía, AP 106, Ensenada 22800, BC, México.*
[3] *Independent Researcher - Via Zoncada 51, 26845 Codogno (LO), Italy.*
[4] *Instituto de Astronomía, UNAM. Ciudad Universitaria 04510, Ciudad de México, México.*

Keywords: *(stars:) binaries: eclipsing, (stars): fundamental parameters, (stars): individual: TIC 9625207, TIC 23081489, TIC 426271738, (techniques): photometric*

Abstract

We present a photometric study and characterization of three contact eclipsing binary systems, analyzed using the Wilson-Devinney code in its Python implementation (`PyWD2015`). Analysis of the CCD-filtered and TESS light curves reveals that two of these systems are totally eclipsing, display starspots and belong to the W-subtype. These systems exhibit good thermal contact with a low degree of overcontact, and their components are consistent with late-type stars. The remaining system is an A-subtype W UMa binary, characterized by a considerable temperature difference between the components (ΔT ~ 2200K) despite a low mass ratio ($q = \frac{M_2}{M_1}$). The times of minima derived from our observations, as well as from optical sky surveys, cover sufficient orbital cycles, allowing us to refine their ephemerides and present O-C diagrams fitted with polynomial functions. Additionally, the orbital angular momentum (J_0) of each system was calculated, and their positions were plotted on the logM-logL and Temperature-Period diagrams for further comparison.

Resumen

Presentamos un estudio fotométrico para la caracterización de tres sistemas binarios eclipsantes en contacto analizados mediante el código Wilson-Devinney bajo una implementación en Phyton (PyWD2015). El análisis de las curvas de luz obtenidas con CCD con filtros y por TESS, revela que dos de estos sistemas son totalmente eclipsantes, presentan manchas estelares y pertenecen al subtipo W. Estos sistemas presentan buen contacto térmico con un grado bajo de sobre-contacto y sus componentes son estrellas de tipo tardio. El otro sistema es una binaria W UMa del subtipo A caracterizada por una considerable diferencia de temperatura de sus componentes (ΔT ~ 2200K) a pesar de su bajo cociente de masas ($q = \frac{M_2}{M_1}$). Los tiempos de mínimo obtenidos con nuestras observaciones y de catastros en el óptico, cubriendo suficientes ciclos orbitales, nos permite refinar sus efemérides y presentar diagramas O-C ajustados con funciones polinomiales. Adicinalmente se calculó el momento angular obital (J_0) de cada sistema y se grafican sus posiciones el los diagramas logM-logL y Temperatura-Periodo para su comparación.

Corresponding author: Francesco Acerbi *E-mail address:* acerbifr@tin.it
Received: September 4, 2025 **Accepted:** November 4, 2025

1. INTRODUCTION

Contact binary systems are generally believed to evolve from detached binaries with orbital periods of a few days. This evolutionary process is primarily driven by the expansion of the component stars and angular momentum loss (AML) mainly through magnetic stellar winds (for example, Eggen & Iben, 1989; Bradstreet & Guinan, 1994; Zhu et al., 2012; Qian et al., 2017). W UMa stars have traditionally been categorized into two primary subclasses: A-type and W-type (Binnendijk, 1965, 1970). A-type systems are distinguished by a primary minimum caused by a transit eclipse, typically featuring earlier spectral types (A-F), longer orbital periods, and a higher degree of contact between components. In contrast, W-type systems exhibit a primary minimum resulting from occultation, generally include later spectral types (G-K), have shorter periods, and possess shallow convective envelopes. The formation mechanisms leading to these two subclasses remain unclear. Li et al. (2008) argued that there is no significant evolutionary distinction between A-type and W-type systems. Yildiz & Doğan (2013) highlighted the role of the initial mass of the secondary star as a key driver in the evolutionary path of binary systems. More recently, Li et al. (2024), analyzing over 11,000 binaries from the All-Sky Automated Survey for Supernovae (ASAS-SN), found evidence that A-type contact binaries evolve differently from W-type binaries. The thermal relaxation oscillation (TRO) theory provides an explanatory framework for this evolution (Lucy, 1967; Flannery, 1976; Robertson & Eggleton, 1977; Yakut & Eggleton, 2005; Li et al., 2008). According to this theory, cyclic oscillations in the thermal structure of the system, driven by mass transfer between the components, cause repeated transitions between the contact and non-contact configurations. In a detached binary system, the more massive component, under the influence of AML and stellar expansion, fills its Roche lobe, initiating mass transfer to the less massive companion and forming a semi-detached system. Ongoing mass transfer leads to orbital shrinkage, culminating in the establishment of a contact binary configuration. The subsequent TRO phase involves a reversal of the mass transfer direction, and the initially less massive component becomes the donor, transferring mass back to its companion. This mass transfer reversal causes the orbit to widen and temporarily disrupt the contact state. Such cycles of mass transfer and orbital evolution repeat over time, with each oscillation accompanied by further loss of mass and angular momentum. Consequently, both the inner and outer Roche lobes shrink progressively, increasing the degree of contact in the system. Ultimately, this evolutionary sequence may produce an extreme-mass-ratio binary, potentially resulting in coalescence. These coalescence events are hypothesized to give rise to FK Com-type stars, blue stragglers, and luminous red novae, exemplified by V1309 Sco (Stępień, 2011; Tylenda et al., 2011; Zhu et al., 2016; Liao et al., 2017).

2. DETAILS ON THE SYSTEMS

TIC 9625207 (RA = $17^h18^m39.92^s$, Dec = $+35°54'25.97''$), also known as V1053 Her, ROTSE1 J171839.88+355423.8, CRTS J171839.89+355426.4 and ZTF J171839.88+355426.6, was first identified as a variable star by Akerlof et al. (2000) during the Robotic Optical Transient Search Experiment I (ROTSE I). It was classified as an eclipsing binary with an orbital period of 0.287801 days, a variation amplitude of Δmag = 0.726, and a quality rating of 8/10. The system was subsequently designated as V1053 Her in the 77th Name List of Variable Stars (Kazarovets et al., 2003). Later studies between 2003 and 2020 refined the orbital period, reporting values ranging from 0.287848 to 0.2877964 days.

TIC 23081489 (2MASS J04021385+2836358; ZTF J040213.86+283636.2; RA = $04^h02^m13.85^s$, Dec = $+28°36'35.83''$, J2000.0) was classified as an EW-type variable star from CSS data (Drake et al., 2014). This study estimated a period of 0.585746 d and a variation amplitude of 0.41 mag, indicating a contact binary system. Subsequent observations from the All-Sky Automated Survey for Supernovae (ASAS-SN) project (Shappee et al., 2014; Jayasinghe et al., 2019) confirmed a period of 0.5857464 d and reported an amplitude of 0.29 mag. Additionally, the ASAS-SN dataset provides a color index (B-V) of 0.580 and an estimated reddening E(B-V) of 0.248.

TIC 426271738 (2MASS J05430504+4056375; RA = $05^h43^m05.05^s$, Dec = $+40°56'37.53''$, J2000.0), also known as ZTF J054301.06+405701.4, SvkV34, and LAMOST J054301.06+405701.5, was discovered by Marian Urbanik in 2012. The orbital period was established as 0.245675 d, and the system was classified as an EW-type eclipsing binary. No further studies have been published since this discovery. The ASAS-SN observations (Shappee et al., 2014; Jayasinghe et al., 2019) reported an amplitude variation Δmag = 0.49 and a refined orbital period of 0.2456753 days.

3. OBSERVATIONS AND DATA REDUCTION

3.1. SPM Observations

All observations were carried out at the San Pedro Mártir Observatory (Mexico) with a 0.84-m telescope (an f/15 Ritchey-Chretien), Mexman filter wheel, and *Marconi 5* CCD detector (an e2v CCD231-42 chip with $15 \times 15\ \mu^2$ pixels, gain of 2.2e$^-$/ADU, and readout noise of 3.6e$^-$). The field of view was $10' \times 10'$ and binning 2×2 was employed during all observations.

TIC 9625207 was observed on 20240610 UT for 3.8h alternating exposures in filters V, R_c and I_c, with exposure times of 100 s, 60 s, and 40 s, respectively. It was observed on 20240629 UT for 7.1 h with filters B, V, R_c and I_c, with exposure times of 90, 70, 40 and 30s respectively.

TIC 23081489 was observed for the first time on 20161108 during 6.7 h alternating filters R_c and I_c with exposure times of 50 and 25 s, respectively. It was then observed on 20161206 for 1.6 h with filters B, $V$and R_c with exposure times of 25 s, 15 s, and 10 s, respectively. On 20180119, it was observed for 5.9 h using filters B, V, R_c and I_c and exposure times of 50, 25, and 20 s, respectively. On 20191130, it was observed for 4.3 h using filters R and I with 50 and 20 s of exposure time, respectively. On 20210930, it was observed with filters B, V, R_c and I_c and exposure times of 50, 25, 20, and 20 s. Lastly, it was observed on 20221105 for 3.5 h with filters R and I and exposure times of 40 s for both cases.

TIC 426271738 was observed on 20171105 for 7.2 h with filters V, R_c and I_c and exposure times of 50, 30, and 20 s, respectively, and with the same conditions for 1 h on 20211020 and for 7.7 h on 20221202.

All images were processed using IRAF[1] routines. Images were bias subtracted and flat-field corrected before the instrumental magnitudes were computed using the standard aperture photometry method.

3.2. TESS data

The Transiting Exoplanet Survey Satellite (TESS) conducts nearly continuous observations, providing time-series data spanning approximately 27.4 days per sector, with only brief interruptions of 1 to 2 days to download the acquired data. The bandpass of each of the four onboard cameras covers the wavelength range from 600 nm to 1000 nm, centered near the Cousins I bandpass with an effective wavelength of 786.5 nm (Ricker et al., 2015). TESS mission data become available after processing by the Science Processing Operations Center (SPOC) and Quick-Look Pipeline (QLP). The SPOC and High-Level Science Products from QLP (HLSP-QLP) can be accessed via the Mikulski Archive for Space Telescopes (MAST) portal[2]. We developed a small custom Python script to query the data availability and automate the download process.

When multiple TESS sectors observed the same system we selected, for light curve fitting, we used the data with the lowest scatter. Our priority order was the Pre-search Data Conditioning Simple Aperture Photometry (PDCSAP) light curves, in which long-term trends are removed along with flux contamination from nearby stars (Smith et al., 2012; Stumpe et al., 2014); the Kepler Science Pipeline Simple Aperture Photometry (KSPSAP), which is normalized and detrended using Kepler splines and Simple Aperture Photometry (SAP), representing background-corrected flux values.

Data points exhibiting obvious deviations or flagged with quality values > 0 (indicating unreliable flux measurements) were excluded from the analysis. The resulting light curves were normalized using flux levels at phase 0.25 or, in the presence of spotted systems, at phases free from spot modulation.

[1] IRAF is distributed by the National Optical Observatories, operated by the Association of Universities for Research in Astronomy, Inc., under cooperative agreement with the National Science Foundation.

[2] https://mast.stsci.edu/portal/Mashup/Clients/Mast/Portal.html

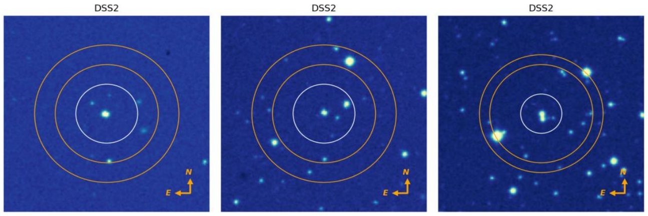

Figure 1. The Digital Sky Survey (DSS2) field of view corresponding to a TESS image of 10x10 pixels. The white circle shows the photometric aperture, and the orange circles show the sky annulus. From left to right: TIC 9625207, TIC 23081489, TIC 426271738.

The downloaded MAST data were jointly fitted to the SPM CCD light curves. When MAST data were unavailable, we extracted light curves using the online tool `TESS.xtractor` (Serna et al., 2021). `TESSExtractor` performs photometry using a circular aperture centered on the target, applies a sky annulus for background subtraction, and corrects for systematics using cotrending basis vectors (CBVs) provided by TESS. Photometric anomalies caused by cosmic rays, popcorn noise, and fireworks events were removed from the raw data using quality flag filtering (Serna et al., 2021), producing light curves that are comparable in quality to the SAP data.

An important quality metric in TESS data is the CROWDSAP parameter (Burke et al. 2023)[3], which quantifies the fraction of the flux in the photometric aperture attributable to the target star after background correction. Low CROWDSAP values indicate significant contamination from nearby stars, thereby reducing the reliability of the variability measurements for the target. For the light curves extracted using `TESSExtractor` (Serna et al., 2021) recommend caution with targets having a Crowding Ratio exceeding 25%.

Among the three systems studied, TIC 9625207 has high CROWDSAP values of 0.947 and 0.951 for Sectors 25 and 26, respectively (based on PDCSAP light curves), indicating that less than 5.3% and 4.9% of the flux in the aperture originates from contaminating sources. For TIC 23081489 and TIC 426271738, the Crowding Ratios obtained through `TESSExtractor` are 147% and 97%, respectively. The first target is free from significant stray light contamination Figure 1.

Due to possible contamination in other light curves, their data were used cautiously and primarily for comparison purposes. The details of the TESS observations are summarized in Table 1.

4. PERIOD ANALISYS

From our observations, we derived new times of minimum (ToM) for all systems. Leveraging the increasing availability of data from various optical sky surveys, we compiled as many eclipse timings as possible to investigate period variations in our target binaries, searching the literature.

The times of minima were determined using the Kwee & van Woerden method (Kwee & van Woerden, 1956), implemented in Python by Deeg (2021). We applied this method to light curves obtained from the ASAS-SN (Shappee et al., 2014; Jayasinghe et al., 2019), CRTS (Drake et al., 2014), Super-Wide Angle Search for Planets (SuperWASP); (Butters et al., 2010), TESS (Ricker et al., 2015), and ZTF (Chen et al., 2020).

Although SuperWASP and TESS (2 min cadence) provide continuous observations, other surveys offer more sporadic coverage. Consequently, ToMs were derived directly from SuperWASP and TESS data, whereas for TESS data with 10 and 30-minute cadences and for the other surveys, the period-shift method proposed by Li et al. (2020) was employed to determine the observed minus calculated (O-C) values.

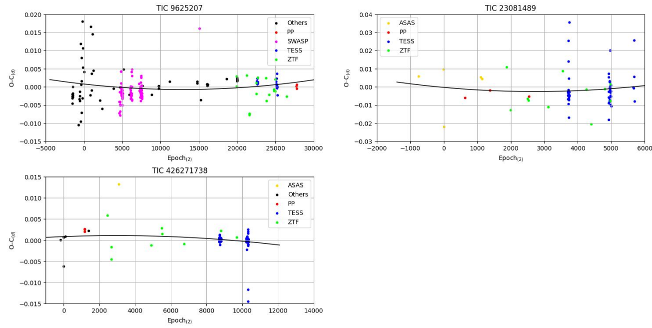

Figure 2. The O-C data points of the minima (colored points) and the polynomial fit (black line).

TESS observations are reported in Barycentric Julian Date (BJD); therefore, Heliocentric Julian Dates (HJD) from other sources were converted to BJD using the online converter hjd2bjd (Eastman et al., 2010)[4]. The resulting O-C data are listed in Table 2, and Figure 2 displays the minima timings along with the second-order polynomial fits. The updated ephemerides derived from these fits are listed in Table 3.

4.1. Secular rate of change periods

Using the well-established relations from Hilditch (2001):

$$\frac{dM_2}{dt} = \frac{M_1 M_2}{3P(M_1 - M_2)} \times \frac{dP}{dt} \tag{1}$$

$$\frac{dM_1}{dt} = \frac{M_1 M_2}{3P\,(M_1 - M_2)} \times \frac{dP}{dt}; \tag{2}$$

The equation for the variation of the mass ratio from Yang & Liu (2003):

$$\frac{\mathrm{d}q}{\mathrm{d}t} = \frac{-q(1+q)}{3p(1-q)}\frac{\mathrm{d}p}{\mathrm{d}t}; \tag{3}$$

and the angular momentum loss (AML) related period change expression from Bradstreet & Guinan (1994):

$$\dot{P} \approx -1.1 \times 10^{-8} q^{-1} (1+q)^2 (M_1 + M_2)^{-\frac{5}{3}} k^2 \left(M_1 R_1^4 - M_2 R_2^4\right) P^{-\frac{7}{3}}. \tag{4}$$

where we adopt k^2=0.1.

We calculated the secular rate of period change (dP/dt) for the studied systems. These values enabled us to derive related parameters, including the mass transfer rates (dM_1/dt, dM_2/dt), indicating whether the mass is transferred from the less massive to the more massive component or vice versa; the rate of change of the mass ratio (dq/dt), which expresses how the mass ratio evolves over time; and the evaluation of whether angular momentum loss (AML) drives the observed period variations, based on dP/dt AML.
The calculated results are summarized in Table 4.

From Table 4, it is evident that the secular rates of period change are increasing for the first two systems and decreasing for the last one. The mass transfer rates are negative for the two systems, indicating that the less massive component, specifically M_1 in

[3]https://archive.stsci.edu/missions/tess/doc/tess_drn/tess_sector_66_drn92_v01.pdf

[4]https://astroutils.astronomy.osu.edu/time/hjd2bjd.html

Table 1. Details of the TESS data.

System	Sector	Year	Author	Exp Time (s)	Used flux
TIC 9625207	25	2020 May 14 to June 08	TESS-SPOC	1800	PDCSAP
	25	2020	QLP	1800	
	26	2020 June 09 to July 07	TESS-SPOC	1800	PDCSAP
	26	2020	QLP	1800	
	52	2022 May 19 to June 12	QLP	600	SAP
	53	2022 June 13 to July 07	QLP	600	KSPSAP
TIC 23081489	44	2021 Oct 12 to Nov 05	TESSExtractor	600	SAP
	70	2023 Sep 20 to Oct 16	TESSExtractor	200	SAP
	71	2023 Oct 16 to Nov 11	TESSExtractor	200	SAP
	86	2024 Nov 21 to Dec 18	TESSExtractor	200	SAP
TIC 426271738	59	2022 Nov 26 to Dec23	QLP	200	SAP
	73	2023 Dec 07 to 2024 Jan 03	QLP	200	SAP

TIC 9625207 and M_2 in TIC 426271738, is losing mass to the more massive companion. Consequently, the mass ratio increased for TIC 9625207, whereas it decreased for the other systems.

5. LIGHT CURVES SOLUTION

We analyzed the TESS and SPM light curves using the 2015 version of the Wilson-Devinney code (Wilson & Devinney, 1971; Wilson, 1990; Wilson, 1994) and Wilson & van Hamme (2016)[5]. For TIC 9625207 and TIC 426271738, QLP data were employed, whereas for the remaining systems, only SPM data were used. The analysis was conducted using the Python interface `PyWD2015` (Güzel & Özdarcan, 2020), which primarily serves as a graphical user interface (GUI) wrapper for the core Wilson-Devinney (WD) code. It does not alter the fundamental functionality of the WD program but offers a user-friendly interface for the Differential Corrections (DC) and Light Curve (LC) modules. `PyWD2015` includes several helpful tools that simplify the technical aspects of modeling and support the iterative visualization of the results. In addition to acting as a WD GUI, it provides additional convenient features that enable users to efficiently assess the fit between observations and initial models. Moreover, it streamlines modifications to the modeling approaches and allows real-time graphical tracking of the results through iterations.

Theoretical light curves were generated by iteratively adjusting the free parameters: the temperature of the secondary component (T_2), orbital inclination (i), monochromatic luminosity of the primary component (L_1), third light contribution (L_3), and dimensionless potentials ($\Omega_{1,2}$). The best fit to the observations was achieved using successive iterations. We applied the standard "q-search" method, initially fixing the mass ratio (q) and gradually increasing its value, while allowing the other free parameters to converge. Once an optimal set of parameters was found, q was released in subsequent iterations to refine the solution.

Other parameters were fixed at theoretical values appropriate for stars with convective envelopes (effective temperature $T <$ 7200K). Following Ruciński (1973), bolometric albedos of A_1=A_2=0.5 were adopted. Gravity-darkening coefficients were set to g_1=g_2=0.32, according to Lucy (1967). The limb-darkening coefficients for both components were interpolated from the square-root law tables by Claret & Bloemen (2011). For the TESS light curves, which cover a broad bandpass of 600-1000 nm centered near the Cousins I band with effective wavelength 786.5 nm (Ricker et al., 2015)), a power-2 limb-darkening model from Claret & Southworth (2023) was used. The temperature of the primary component (T_1) was fixed throughout the Wilson-Devinney analyses. For each system, T_1 was assigned as follows:

TIC 9625207: Values of T_1=5398 K, was adopted from the Gaia DR3 catalog (Gaia Collaboration et al., 2023), flagged with high-quality data (quality flag = 1; Avdeeva et al., 2024). This value exceeds the mean temperatures reported in the `VizieR` catalog by only 100 K and was preferred.

TIC 23081489: Temperatures from the TESS Input Catalog 8.2 (Paegert et al., 2021) and LAMOST DR7 (Luo et al., 2019) are consistent, reporting T_1=6971.6 K and 6974.9 K respectively. This aligns with the temperature estimated from the dereddened $(B-V)_0$=0.332 color index obtained from ASAS-SN data (Shappee et al., 2014; Jayasinghe et al., 2019), corresponding to T_1=6967 K using Pecaut & Mamajek (2013) tables. We adopted a final value of T_1=6970 K.

TIC 426271738: LAMOST DR7 (Luo et al., 2019) reports T_1=4556 K, while Qian et al. (2020) give T_1=4537 K with a spectral type of K5. Using the tables of Pecaut & Mamajek (2013), the K5 spectral type corresponds to T_1=4440 K. We adopted an average value T_1=4500 K for our analysis. In this study, the components of the binary systems exhibiting higher temperatures were designated as primary.

The light curves of all systems, except TIC 23081489, exhibit features characteristic of W UMa-type contact binaries. Accordingly, our initial analysis of these systems was performed using `Mode 3` of the Wilson-Devinney (W-D) code, which is specifically designed for overcontact binary systems in which both stellar components completely fill their respective Roche lobes. Although stars share a common envelope, they may exhibit different surface brightnesses due to geometric contact without achieving thermal equilibrium.

For TIC 23081489, possible semi-detached configurations were considered by exploring additional modes of interaction. Alongside `Mode 3`, we tested `Modes 4` and `5`, corresponding to configurations where stars 1 or 2 filled their Roche lobes, respectively. However, the solutions in `Mode 4` failed to converge;

[5] ftp.astro.ufl.edu directory pub/wilson/lcdc2015

Table 2. A sample of the times of minima extracted from SPM observations and Surveys data.

Target	BJD	Epoch(1)	O-C (1)	Epoch(2)	O-C (2)	Error	Source*	Filter
TIC 9625207	2452056.39518	-1542	−0.0082	−1542	−0.0046		Blättler (2001)	ccd
	2452056.54056	-1541.5	-0.0067	-1541.5	-0.0031		Blättler (2001a)	CCD clear
	2452058.55556	-1534.5	-0.0063	-1534.5	-0.0027		Blättler (2001a)	CCD clear
	2452065.46336	-1510.5	-0.0056	-1510.5	-0.002		Blättler (2001a)	CCD clear
	2452073.37746	-1483	-0.0059	-1483	-0.0023		Blättler (2001a)	CCD clear
	2452073.52086	-1482.5	-0.0064	-1482.5	-0.0028		Blättler (2001a)	CCD clear
	2452075.39436	-1476	-0.0036	-1476	0		Blättler (2001a)	CCD clear
	2452075.53646	-1475.5	-0.0053	-1475.5	-0.0018		Blättler (2001a)	CCD clear
	2452296.69876	-707	-0.0144	-707	-0.0105		Locher (2002)	Visual
	2452323.61476	-613.5	-0.0073	-613.5	-0.0034		Locher (2002)	Visual
	2452344.62476	-540.5	-0.0064	-540.5	-0.0025		Locher (2002)	Visual
	2452345.63076	-537	-0.0077	-537	-0.0038		Locher (2002)	Visual
	2452347.64776	-530	-0.0053	-530	-0.0013		Locher (2002)	Visual
	2452370.54076	-450.5	0.0079	-450.5	0.0119		Locher (2002)	Visual
	2452382.60676	-408.5	-0.0135	-408.5	-0.0095		Locher (2002a)	Visual
	2452395.42376	-364	-0.0034	-364	0.0006		Locher (2002a)	Visual
	2452409.52676	-315	-0.0025	-315	0.0016		Locher (2002a)	Visual
	2452411.54776	-308	0.004	-308	0.008		Locher (2002a)	Visual
	2452415.56176	-294	-0.0112	-294	-0.0071		Locher (2002a)	Visual
	2452438.46676	-214.5	0.014	-214.5	0.0181		Locher (2002a)	Visual
	2452442.47476	-200.5	-0.0071	-200.5	-0.0031		Blättler (2002)	CCD clear
	2452460.47576	-138	0.0066	-138	0.0107		Locher (2002a)	Visual
	2452465.50676	-120.5	0.0012	-120.5	0.0053		Locher (2002a)	Visual
	2452500.18501	0	0	0	0.0041		VSX	
	2452708.56975	724	0.0204	724	0.0248		Locher (2003)	Visual
	2452745.52445	852.5	-0.0067	852.5	-0.0023		Blättler (2003)	CCD clear
	2452752.60475	877	0.0225	877	0.027		Locher (2003)	Visual
	2452753.45775	880	0.0122	880	0.0166		Locher (2003)	Visual
	2452783.51475	984.5	-0.0055	984.5	-0.001		Locher (2003)	Visual
	2452791.57775	1012.5	-0.0008	1012.5	0.0037		Locher (2003)	Visual
	2452812.45375	1085	0.01	1085	0.0145		Locher (2003)	Visual
	2452850.43275	1217	-0.0001	1217	0.0045		Locher (2004)	Visual
	2453096.48995	2072	-0.0086	2072	-0.0037		Blättler (2004)	CCD clear
	2453186.56774	2385	-0.011	2385	-0.006		Locher (2005)	Visual
	2453614.38164	3871.5	-0.0061	3871.5	-0.0005		Blättler (2006)	CCD clear
	2453830.65653	4623	-0.01	4623	-0.0041	0.0016	SWASP 146	
	2453832.66799	4630	-0.0131	4630	-0.0072	0.0003	SWASP 146	
	2453833.68108	4633.5	-0.0073	4633.5	-0.0014	0.0006	SWASP 145	
	2453851.66569	4696	-0.0099	4696	-0.0041	0.0004	SWASP 145	
	2453853.67935	4703	-0.0109	4703	-0.005	0.0007	SWASP 146	
	2453855.54829	4709.5	-0.0126	4709.5	-0.0067	0.0004	SWASP 145	
	2453855.69105	4710	-0.0137	4710	-0.0078	0.0003	SWASP 145	
	2453856.55743	4713	-0.0107	4713	-0.0048	0.0003	SWASP 145	
	2453863.46924	4737	-0.006	4737	-0.0001		Agerer (2006)	CCD Ir
	2453884.47821	4810	-0.0062	4810	-0.0003	0.0007	SWASP 143	
	2453885.48675	4813.5	-0.0049	4813.5	0.001	0.0008	SWASP 143	
	2453885.63385	4814	-0.0017	4814	0.0042	0.0009	SWASP 146	
	2453887.50463	4820.5	-0.0016	4820.5	0.0043	0.0465	SWASP 143	
	2453901.45762	4869	-0.0067	4869	-0.0008	0.0003	SWASP 142	
	2453901.60025	4869.5	-0.008	4869.5	-0.0021	0.0005	SWASP 146	

Table 2. Continued

Target	BJD	Epoch(1)	O-C (1)	Epoch(2)	O-C (2)	Error	Source*	Filter
	2453902.46517	4872.5	-0.0065	4872.5	-0.0005	0.0004	SWASP 142	
	2453903.47104	4876	-0.0079	4876	-0.0019	0.0002	SWASP 145	
	2453903.47121	4876	-0.0077	4876	-0.0018	0.0003	SWASP 142	
	2453903.61688	4876.5	-0.0059	4876.5	0	0.0006	SWASP 142	
	2453904.47875	4879.5	-0.0075	4879.5	-0.0015	0.0004	SWASP 142	
	2453904.47899	4879.5	-0.0072	4879.5	-0.0013	0.0005	SWASP 145	
	2453904.62181	4880	-0.0083	4880	-0.0024	0.0004	SWASP 145	
	2453906.49330	4886.5	-0.0075	4886.5	-0.0015	0.0005	SWASP 146	
	2453907.50023	4890	-0.0078	4890	-0.0019	0.0003	SWASP 145	
	2453907.50074	4890	-0.0073	4890	-0.0014	0.0009	SWASP 146	
	2453920.59636	4935.5	-0.0064	4935.5	-0.0005	0.0007	SWASP 146	
	2453921.45872	4938.5	-0.0075	4938.5	-0.0015	0.0004	SWASP 146	
	2453921.45917	4938.5	-0.007	4938.5	-0.0011	0.0004	SWASP 145	
	2453922.46662	4942	-0.0069	4942	-0.0009	0.0004	SWASP 145	
	2453923.47343	4945.5	-0.0073	4945.5	-0.0014	0.0006	SWASP 145	
	2453938.43931	4997.5	-0.0069	4997.5	-0.0009	0.0002	SWASP 145	
	2453942.46642	5011.5	-0.0089	5011.5	-0.0029	0.0004	SWASP 145	
	2453944.48066	5018.5	-0.0092	5018.5	-0.0032	0.0003	SWASP 145	
	2453945.48618	5022	-0.011	5022	-0.005	0.0006	SWASP 142	
	2453946.49603	5025.5	-0.0084	5025.5	-0.0024	0.0002	SWASP 142	
	2453947.50298	5029	-0.0088	5029	-0.0028	0.0005	SWASP 142	
	2453948.51123	5032.5	-0.0078	5032.5	-0.0018	0.0002	SWASP 145	
	2453984.50950	5157.5	0.016	5157.5	0.022	0.0001	SWASP 146	
	2453992.40674	5185	-0.0012	5185	0.0049		Blättler (2007)	CCD clear
	2454202.49064	5915	-0.0085	5915	-0.0021		Blättler (2007)	CCD clear
	2454228.53777	6005.5	-0.0069	6005.5	-0.0005	0.0016	SWASP 146	
	2454249.54748	6078.5	-0.0063	6078.5	0.0001	0.0002	SWASP 146	
	2454252.56693	6089	-0.0087	6089	-0.0023	0.0008	SWASP 146	
	2454254.43840	6095.5	-0.0079	6095.5	-0.0015	0.0009	SWASP 146	
	2454254.72676	6096.5	-0.0074	6096.5	-0.001	0.0001	SWASP 146	
	2454260.48030	6116.5	-0.0097	6116.5	-0.0033	0.0001	SWASP 146	
	2454262.49554	6123.5	-0.0091	6123.5	-0.0027	0.0002	SWASP 146	
	2454262.64192	6124	-0.0066	6124	-0.0002	0.0003	SWASP 146	
	2454263.50215	6127	-0.0097	6127	-0.0033	0.0001	SWASP 146	
	2454264.51084	6130.5	-0.0083	6130.5	-0.0019	0.0003	SWASP 146	
	2454275.59092	6169	-0.0084	6169	-0.002	0.0002	SWASP 142	
	2454279.62615	6183	-0.0023	6183	0.0041	0.0489	SWASP 142	
	2454284.51268	6200	-0.0083	6200	-0.0019	0.0008	SWASP 146	
	2454287.53402	6210.5	-0.0089	6210.5	-0.0024	0.0001	SWASP 142	
	2454289.54920	6217.5	-0.0082	6217.5	-0.0018	0.0005	SWASP 142	
	2454294.58376	6235	-0.0101	6235	-0.0037	0.0201	SWASP 142	
	2454296.45810	6241.5	-0.0065	6241.5	0	0.0004	SWASP 142	
	2454298.46919	6248.5	-0.0099	6248.5	-0.0035	0.0005	SWASP 142	
	2454303.51386	6266	-0.0017	6266	0.0048	0.0007	SWASP 142	
	2454307.54119	6280	-0.0035	6280	0.003	0.0379	SWASP 142	
	2454558.64090	7152.5	-0.0059	7152.5	0.0009	0.0006	SWASP 146	
	2454580.65534	7229	-0.0079	7229	-0.0011	0.0009	SWASP 147	
	2454613.60799	7343.5	-0.0079	7343.5	-0.001	0.0006	SWASP 146	
	2454616.63049	7354	-0.0073	7354	-0.0004	0.0003	SWASP 146	
	2454619.64984	7364.5	-0.0098	7364.5	-0.0029	0.0004	SWASP 146	

Table 2. Continued

Target	BJD	Epoch(1)	O-C (1)	Epoch(2)	O-C (2)	Error	Source*	Filter
	2454620.51548	7367.5	-0.0075	7367.5	-0.0006	0.0003	SWASP 146	
	2454620.65842	7368	-0.0085	7368	-0.0016	0.0003	SWASP 146	
	2454621.52051	7371	-0.0098	7371	-0.0029	0.0004	SWASP 146	
	2454622.53068	7374.5	-0.0069	7374.5	0	0.0004	SWASP 146	
	2454623.53653	7378	-0.0083	7378	-0.0014	0.0003	SWASP 146	
	2454625.55196	7385	-0.0075	7385	-0.0006	0.0005	SWASP 146	
	2454626.55937	7388.5	-0.0073	7388.5	-0.0005	0.0005	SWASP 146	
	2454628.57420	7395.5	-0.0071	7395.5	-0.0002	0.0003	SWASP 146	
	2454629.43398	7398.5	-0.0107	7398.5	-0.0038	0.0006	SWASP 146	
	2454629.58051	7399	-0.0081	7399	-0.0012	0.0007	SWASP 146	
	2454630.58843	7402.5	-0.0074	7402.5	-0.0005	0.0004	SWASP 146	
	2454631.45214	7405.5	-0.0071	7405.5	-0.0002		Agerer (2009)	CCD Ir
	2454635.62326	7420	-0.009	7420	-0.0021	0.0665	SWASP 146	
	2454637.64121	7427	-0.0057	7427	0.0012	0.0004	SWASP 147	
	2454641.52539	7440.5	-0.0067	7440.5	0.0002	0.0005	SWASP 147	
	2454643.53745	7447.5	-0.0092	7447.5	-0.0023	0.0004	SWASP 147	
	2454644.54510	7451	-0.0089	7451	-0.002	0.0009	SWASP 146	
	2454645.40776	7454	-0.0096	7454	-0.0027	0.0002	SWASP 146	
	2454647.42378	7461	-0.0081	7461	-0.0012	0.0004	SWASP 146	
	2454647.56816	7461.5	-0.0077	7461.5	-0.0008	0.0005	SWASP 146	
	2454648.57926	7465	-0.0039	7465	0.0031	0.0329	SWASP 147	
	2454648.72273	7465.5	-0.0043	7465.5	0.0026	0.0001	SWASP 147	
	2454649.58210	7468.5	-0.0083	7468.5	-0.0014	0.0002	SWASP 146	
	2454652.46055	7478.5	-0.0078	7478.5	-0.0009	0.0002	SWASP 146	
	2454664.40538	7520	-0.0065	7520	0.0004	0.0455	SWASP 146	
	2454669.44058	7537.5	-0.0078	7537.5	-0.0008	0.0002	SWASP 146	
	2454671.45416	7544.5	-0.0087	7544.5	-0.0018	0.0002	SWASP 146	
	2454672.46021	7548	-0.01	7548	-0.003	0.0003	SWASP 146	
	2454675.48266	7558.5	-0.0094	7558.5	-0.0025	0.0004	SWASP 147	
	2454675.48329	7558.5	-0.0088	7558.5	-0.0018	0.0003	SWASP 146	
	2454678.50372	7569	-0.0102	7569	-0.0032	0.0005	SWASP 146	
	2454686.41859	7596.5	-0.0097	7596.5	-0.0028	0.0005	SWASP 147	
	2454697.50174	7635	-0.0067	7635	0.0003		Blättler (2009)	CCD clear
	2455049.47346	8858	-0.0097	8858	-0.0022		Blättler (2010)	CCD clear
	2455312.80906	9773	-0.0075	9773	0.0002		Diethelm (2010)	CCD V
	2455314.39116	9778.5	-0.0083	9778.5	-0.0005		Agerer (2011)	CCD Ir
	2455314.53586	9779	-0.0075	9779	0.0003		Agerer (2011)	CCD Ir
	2455722.77537	11197.5	-0.0068	11197.5	0.0015		Diethelm (2011)	CCD V
	2456764.45158	14817	-0.0087	14817	0.001	0.0017	Agerer (2015)	CCD Ir
	2456764.59598	14817.5	-0.0082	14817.5	0.0015	0.0007	Agerer (2015)	CCD Ir
	2456833.68156	15057.5	0.0063	15057.5	0.0161	0.0008	SWASP 146	
	2456881.86771	15225	-0.0134	15225	-0.0036		ASASSN	
	2457112.54036	16026.5	-0.0093	16026.5	0.0008		Magris M.	CCD V
	2457131.39088	16092	-0.0094	16092	0.0007	0.0001	Moschner & Frank (2016)	CCD clear
	2457136.57088	16110	-0.0098	16110	0.0003	0.0007	Moschner & Frank (2016)	CCD V
	2457158.44357	16186	-0.0096	16186	0.0006	0.0001	Moschner & Frank (2016)	CCD clear
	2457852.60858	18598	-0.0088	18598	0.0022		Moschner (2018)	CCD V
	2458231.92407	19916	-0.0087	19916	0.0029	0.0075	ZTF g’	
	2458246.88664	19968	-0.0115	19968	0.0001	0.0119	ZTF r’	
	2458247.89625	19971.5	-0.0092	19971.5	0.0024		Alton (2019)	Average B,V,Ic

Table 2. Continued

Target	BJD	Epoch(1)	O-C (1)	Epoch(2)	O-C (2)	Error	Source*	Filter
	2458248.90295	19975	-0.0097	19975	0.0018		Alton (2019)	Average B,V,Ic
	2458251.78118	19985	-0.0095	19985	0.0021		Alton (2019)	Average B,V,Ic
	2458251.92475	19985.5	-0.0098	19985.5	0.0017		Alton (2019)	Average B,V,Ic
	2458255.81025	19999	-0.0096	19999	0.002		Alton (2019)	Average B,V,Ic
	2458255.95371	19999.5	-0.01	19999.5	0.0016		Alton (2019)	Average B,V,Ic
	2458612.96599	21240	-0.0088	21240	0.0032	0.0101	ZTF r'	
	2458723.75689	21625	-0.0194	21625	-0.0073	0.0101	ZTF g'	
	2458723.90039	21625.5	-0.0198	21625.5	-0.0077	0.0107	ZTF g'	
	2458986.81057	22539	-0.0114	22539	0.0011	0.0129	ZTF r'	
	2458986.95152	22539.5	-0.0143	22539.5	-0.0019	0.0003	ZTF r'	
	2458993.43034	22562	-0.0109	22562	0.0016	0.0006	TESS S25	
	2458993.57381	22562.5	-0.0114	22562.5	0.0011	0.0001	TESS S25	
	2459008.97206	22616	-0.0102	22616	0.0023	0.0002	TESS S25	
	2459010.40954	22621	-0.0117	22621	0.0008	0.0001	TESS S26	
	2459025.95103	22675	-0.0112	22675	0.0013	0.0002	TESS S26	
	2459026.09458	22675.5	-0.0116	22675.5	0.001	0.0001	TESS S52	
	2459033.72283	22702	-0.0099	22702	0.0026	0.0011	ZTF g'	
	2459335.90814	23752	-0.0105	23752	0.0024	0.0129	ZTF g'	
	2459352.88189	23811	-0.0168	23811	-0.0038	0.0161	ZTF i'	
	2459452.74863	24158	-0.0153	24158	-0.0022	0.0194	ZTF r'	
	2459638.95359	24805	-0.0144	24805	-0.0011	0.0149	ZTF g'	
	2459639.09790	24805.5	-0.014	24805.5	-0.0007	0.0004	ZTF g'	
	2459685.86415	24968	-0.0146	24968	-0.0012	0.0142	ZTF r'	
	2459686.01137	24968.5	-0.0113	24968.5	0.0021	0.0005	ZTF r'	
	2459725.00644	25104	-0.0126	25104	0.0008	0.0041	TESS S52	
	2459725.15096	25104.5	-0.012	25104.5	0.0015	0.0001	TESS S52	
	2459732.20094	25129	-0.013	25129	0.0004	0.0087	TESS S52	
	2459738.53426	25151	-0.0112	25151	0.0023	0.0046	TESS S52	
	2459744.57590	25172	-0.0133	25172	0.0002	0.0147	TESS S53	
	2459754.36050	25206	-0.0138	25206	-0.0003	0.0187	TESS S53	
	2459754.50522	25206.5	-0.0129	25206.5	0.0006	0.0007	TESS S53	
	2459757.24240	25216	-0.0098	25216	0.0037	0.0138	TESS S53	
	2459767.31162	25251	-0.0135	25251	0	0.0192	TESS S53	
	2459767.45315	25251.5	-0.0158	25251.5	-0.0023	0.0008	TESS S53	
	2460117.84415	26469	-0.0166	26469	-0.0027	0.0137	ZTF r'	
	2460471.83568	27699	-0.0143	27699	0.0001	9E-05	Present Paper	Average V,R,I
	2460490.68572	27764.5	-0.0149	27764.5	-0.0005	7E-05	Present Paper	Average B,V,R,I
	2460490.83070	27765	-0.0138	27765	0.0006	4E-05	Present Paper	Average B,V,R,I
TIC 23081489	2456885.07959	-758	0.0317	-758	0.0059	0.0211	ASAS_SN	
	2457320.87581	-14	0.0326	-14	0.0097	0.0162	ASAS_SN	
	2457329.04446	0	0.0008	0	-0.0220	0.0044	ASAS-SN	
	2457701.00704	635	0.0144	635	-0.0059	0.0003	Present Paper	Average V,I
	2457978.07441	1108	0.0237	1108	0.0053	0.0168	ASAS_SN	
	2457997.98896	1142	0.0229	1142	0.0045	0.0133	ASAS_SN	
	2458137.68211	1380.5	0.0155	1380.5	-0.0019	0.0001	Present Paper	Average B,V,R,I
	2458423.83024	1869	0.0266	1869	0.0110	0.0077	ZTF r'	
	2458494.68139	1990	0.0024	1990	-0.0127	0.0066	ZTF g'	
	2458794.00183	2501	0.0064	2501	-0.0066	0.0088	ZTF r'	
	2458806.88727	2523	0.0054	2523	-0.0075	0.0089	ZTF g'	
	2458815.67552	2538	0.0075	2538	-0.0054	0.0002	Present Paper	Average V,I

Table 2. Continued

Target	BJD	Epoch(1)	O-C (1)	Epoch(2)	O-C (2)	Error	Source*	Filter
	2459151.88595	3112	-0.0005	3112	-0.0112	0.0069	ZTF g'	
	2459411.97559	3556	0.0177	3556	0.0088	0.0092	ZTF r'	
	2459501.28570	3708.5	0.0015	3708.5	-0.0068	0.0042	TESS S44	
	2459502.16639	3710	0.0036	3710	-0.0047	0.0023	TESS S44	
	2459502.75369	3711	0.0051	3711	-0.0032	0.0023	TESS S44	
	2459503.34015	3712	0.0059	3712	-0.0025	0.0011	TESS S44	
	2459504.80298	3714.5	0.0043	3714.5	-0.0040	0.0026	TESS S44	
	2459506.55483	3717.5	-0.0011	3717.5	-0.0094	0.0031	TESS S44	
	2459506.85536	3718	0.0066	3718	-0.0017	0.0014	TESS S44	
	2459507.43942	3719	0.0049	3719	-0.0034	0.0015	TESS S44	
	2459508.33545	3720.5	0.0223	3720.5	0.0140	0.0093	TESS S44	
	2459509.51834	3722.5	0.0337	3722.5	0.0254	0.0055	TESS S44	
	2459513.57630	3729.5	-0.0086	3729.5	-0.0168	0.0031	TESS S44	
	2459514.46472	3731	0.0012	3731	-0.0070	0.0014	TESS S44	
	2459514.75858	3731.5	0.0022	3731.5	-0.0060	0.0015	TESS S44	
	2459516.22171	3734	0.001	3734	-0.0072	0.0012	TESS S44	
	2459516.52649	3734.5	0.0129	3734.5	0.0047	0.0058	TESS S44	
	2459517.50142	3736	0.1092	3736	0.1010	0.0035	TESS S44	
	2459519.73859	3740	0.0034	3740	-0.0048	0.0012	TESS S44	
	2459520.32405	3741	0.0031	3741	-0.0051	0.0014	TESS S44	
	2459520.91213	3742	0.0054	3742	-0.0028	0.0013	TESS S44	
	2459522.08189	3744	0.0037	3744	-0.0045	0.0014	TESS S44	
	2459522.41483	3744.5	0.0438	3744.5	0.0356	0.0009	TESS S44	
	2459821.98527	4256	0.0049	4256	-0.0013	0.0064	ZTF r'	
	2459909.82734	4406	-0.015	4406	-0.0206	0.0073	ZTF g'	
	2460142.97223	4804	0.0029	4804	-0.0012	0.0074	ZTF r'	
	2460209.15649	4917	-0.0022	4917	-0.0058	0.0006	TESS S70	
	2460209.73931	4918	-0.0051	4918	-0.0088	0.0008	TESS S70	
	2460210.31577	4919	-0.0144	4919	-0.0180	0.0016	TESS S70	
	2460210.91704	4920	0.0011	4920	-0.0025	0.0006	TESS S70	
	2460215.61086	4928	0.0089	4928	0.0054	0.0009	TESS S70	
	2460216.19843	4929	0.0108	4929	0.0072	0.0009	TESS S70	
	2460218.52822	4933	-0.0024	4933	-0.0060	0.0008	TESS S70	
	2460219.11158	4934	-0.0048	4934	-0.0084	0.0008	TESS S70	
	2460225.56620	4945	0.0066	4945	0.0031	0.0010	TESS S70	
	2460227.32315	4948	0.0063	4948	0.0028	0.0007	TESS S70	
	2460228.48466	4950	-0.0037	4950	-0.0072	0.0013	TESS S70	
	2460230.83417	4954	0.0028	4954	-0.0006	0.0007	TESS S70	
	2460232.59000	4957	0.0014	4957	-0.0020	0.0008	TESS S70	
	2460237.27840	4965	0.0039	4965	0.0004	0.0008	TESS S71	
	2460237.88371	4966	0.0234	4966	0.0200	0.0017	TESS S71	
	2460240.20174	4970	-0.0015	4970	-0.0049	0.0008	TESS S71	
	2460240.79158	4971	0.0026	4971	-0.0008	0.0006	TESS S71	
	2460244.29710	4977	-0.0064	4977	-0.0098	0.0006	TESS S71	
	2460244.88490	4978	-0.0043	4978	-0.0077	0.0046	ZTF g'	
	2460244.88959	4978	0.0004	4978	-0.0030	0.0009	TESS S71	
	2460245.18685	4978.5	0.0047	4978.5	0.0014	0.0089	ZTF g'	
	2460249.57953	4986	0.0043	4986	0.0010	0.0006	TESS S71	
	2460251.91915	4990	0.001	4990	-0.0024	0.0011	TESS S71	

Table 2. Continued

Target	BJD	Epoch(1)	O-C (1)	Epoch(2)	O-C (2)	Error	Source*	Filter
	2460254.25926	4994	-0.0019	4994	-0.0052	0.0005	TESS S71	
	2460257.18270	4999	-0.0072	4999	-0.0105	0.0009	TESS S71	
	2460640.85441	5654	0.0006	5654	-0.0001	0.0007	TESS S86	
	2460647.88260	5666	-0.0002	5666	-0.0008	0.0016	TESS S86	
	2460659.33117	5685.5	0.0264	5685.5	0.0257	0.0009	TESS S86	
	2460660.77540	5688	0.0062	5688	0.0056	0.0007	TESS S86	
	2460661.93333	5690	-0.0073	5690	-0.0079	0.0008	TESS S86	
	HJD							
TIC 426271738	2456008.32293	-7180.5	0.0046	-7180.5	-0.003		O-C Gateway - Urban¡k M.	CCD Clear
	2456009.30797	-7176.5	0.0069	-7176.5	-0.0007		O-C Gateway - Urban¡k M.	CCD Clear
	2456010.28940	-7172.5	0.0056	-7172.5	-0.0019		O-C Gateway - Urban¡k M.	CCD Clear
	2456011.39521	-7168	0.0059	-7168	-0.0017		O-C Gateway - Urban¡k M.	CCD Clear
	2456269.47670	-6117.5	0.0058	-6117.5	-0.0015		O-C Gateway - Urban¡k M.	CCD Clear
	2456271.32183	-6110	0.0084	-6110	0.001		O-C Gateway - Urban¡k M.	CCD Clear
	2457728.41816	-179	0.0063	-179	0.0001		O-C Gateway - Urban¡k M.	CCD Clear
	2457772.27170	-0.5	0.0068	-0.5	0.0007		O-C Gateway - Urban¡k M.	CCD Clear
	2457772.38769	0	0	0	-0.0062		VSX	
	2457799.41896	110	0.007	110	0.0009		O-C Gateway - Urban¡k M.	CCD Clear
	2458062.78412	1182	0.0086	1182	0.0027		Present Paper	Average V,R,I
	2458062.90689	1182.5	0.0085	1182.5	0.0026		Present Paper	Average V,R,I
	2458063.02915	1183	0.0079	1183	0.002		Present Paper	Average V,R,I
	2458113.26980	1387.5	0.008	1387.5	0.0022		O-C Gateway - Urban¡k M.	CCD Clear
	2458376.02271	2457	0.0115	2457	0.0059	0.0203	ZTF r	
	2458427.85265	2668	0.004	2668	-0.0016	0.0200	ZTF g	
	2458427.97254	2668.5	0.0011	2668.5	-0.0045	0.0047	ZTF r	
	2458533.01071	3096	0.0132	3096	0.0077	0.0244	ASAS_SN	
	2458978.65597	4910	0.004	4910	-0.0012	0.0126	ZTF r	
	2459122.87115	5497	0.008	5497	0.0029	0.0147	ZTF g	
	2459129.99432	5526	0.0066	5526	0.0015	0.0145	ZTF r	
	2459427.99545	6739	0.0039	6739	-0.0009	0.0149	ZTF r	
	2459911.48484	8707	0.0049	8707	0.0005	0.0002	TESS S59	
	2459911.60712	8707.5	0.0043	8707.5	-0.0001	0.0001	TESS S59	
	2459911.73043	8708	0.0048	8708	0.0004	0.0001	TESS S59	
	2459911.85263	8708.5	0.0042	8708.5	-0.0002	0.0002	TESS S59	
	2459912.46754	8711	0.0049	8711	0.0005	0.0001	TESS S59	
	2459912.58986	8711.5	0.0044	8711.5	0	0.0002	TESS S59	
	2459912.71317	8712	0.0049	8712	0.0004	0.0001	TESS S59	
	2459912.95893	8713	0.0049	8713	0.0005	0.0001	TESS S59	
	2459913.08109	8713.5	0.0043	8713.5	-0.0001	0.0002	TESS S59	
	2459913.20441	8714	0.0047	8714	0.0003	0.0001	TESS S59	
	2459913.32680	8714.5	0.0043	8714.5	-0.0001	0.0002	TESS S59	
	2459913.57222	8715.5	0.004	8715.5	-0.0004	0.0002	TESS S59	
	2459913.94158	8717	0.0049	8717	0.0005	0.0001	TESS S59	
	2459914.18739	8718	0.005	8718	0.0006	0.0001	TESS S59	
	2459914.43289	8719	0.0049	8719	0.0004	0.0001	TESS S59	
	2459914.80084	8720.5	0.0043	8720.5	-0.0001	0.0002	TESS S59	
	2459914.92414	8721	0.0048	8721	0.0003	0.0002	TESS S59	
	2459915.04642	8721.5	0.0042	8721.5	-0.0002	0.0002	TESS S59	
	2459915.16898	8722	0.0039	8722	-0.0005	0.0002	TESS S59	

Table 2. Continued

Target	BJD	Epoch(1)	O-C (1)	Epoch(2)	O-C (2)	Error	Source*	Filter
	2459915.29292	8722.5	0.005	8722.5	0.0006	0.0002	TESS S59	
	2459915.53745	8723.5	0.0039	8723.5	-0.0005	0.0002	TESS S59	
	2459915.66103	8724	0.0046	8724	0.0002	0.0001	TESS S59	
	2459915.78368	8724.5	0.0044	8724.5	0		Present Paper	Average V,R,I,
	2459915.90658	8725	0.0045	8725	0.0001		Present Paper	Average V,R,I,
	2459916.02894	8725.5	0.004	8725.5	-0.0004		Present Paper	Average V,R,I,
	2459916.15347	8726	0.0057	8726	0.0013	0.0002	TESS S59	
	2459916.27486	8726.5	0.0043	8726.5	-0.0001	0.0004	TESS S59	
	2459916.39897	8727	0.0055	8727	0.0011	0.0002	TESS S59	
	2459916.52098	8727.5	0.0047	8727.5	0.0003	0.0002	TESS S59	
	2459917.01201	8729.5	0.0044	8729.5	0	0.0001	TESS S59	
	2459917.13531	8730	0.0048	8730	0.0004	0.0001	TESS S59	
	2459917.25777	8730.5	0.0045	8730.5	0.0001	0.0002	TESS S59	
	2459917.50334	8731.5	0.0044	8731.5	0	0.0001	TESS S59	
	2459917.62657	8732	0.0048	8732	0.0004	0.0001	TESS S59	
	2459917.87226	8733	0.0048	8733	0.0004	0.0001	TESS S59	
	2459918.24067	8734.5	0.0047	8734.5	0.0003	0.0001	TESS S59	
	2459918.36372	8735	0.0049	8735	0.0005	0.0001	TESS S59	
	2459918.60928	8736	0.0048	8736	0.0004	0.0001	TESS S59	
	2459918.73162	8736.5	0.0043	8736.5	-0.0001	0.0001	TESS S59	
	2459918.85495	8737	0.0048	8737	0.0004	0.0002	TESS S59	
	2459918.97732	8737.5	0.0043	8737.5	-0.0001	0.0001	TESS S59	
	2459919.22313	8738.5	0.0044	8738.5	0	0.0002	TESS S59	
	2459919.96007	8741.5	0.0043	8741.5	-0.0001	0.0001	TESS S59	
	2459920.08333	8742	0.0048	8742	0.0004	0.0001	TESS S59	
	2459920.32901	8743	0.0048	8743	0.0004	0.0001	TESS S59	
	2459920.45141	8743.5	0.0043	8743.5	-0.0001	0.0001	TESS S59	
	2459920.57476	8744	0.0049	8744	0.0004	0.0001	TESS S59	
	2459920.69735	8744.5	0.0046	8744.5	0.0002	0.0002	TESS S59	
	2459920.82037	8745	0.0048	8745	0.0004	0.0001	TESS S59	
	2459920.94291	8745.5	0.0045	8745.5	0.0001	0.0002	TESS S59	
	2459921.18818	8746.5	0.0041	8746.5	-0.0003	0.0002	TESS S59	
	2459921.67981	8748.5	0.0044	8748.5	0	0.0002	TESS S59	
	2459921.80301	8749	0.0047	8749	0.0003	0.0001	TESS S59	
	2459922.17010	8750.5	0.0033	8750.5	-0.0011	0.0002	TESS S59	
	2459922.41749	8751.5	0.005	8751.5	0.0006	0.0003	TESS S59	
	2459922.54018	8752	0.0049	8752	0.0005	0.0002	TESS S59	
	2459925.11931	8762.5	0.0044	8762.5	0	0.0002	TESS S59	
	2459925.48803	8764	0.0046	8764	0.0002	0.0002	TESS S59	
	2459925.85639	8765.5	0.0045	8765.5	0.0001	0.0002	TESS S59	
	2459925.97953	8766	0.0048	8766	0.0004	0.0000	TESS S59	
	2459926.47102	8768	0.0049	8768	0.0005	0.0001	TESS S59	
	2459926.83889	8769.5	0.0043	8769.5	-0.0001	0.0001	TESS S59	
	2459927.08480	8770.5	0.0045	8770.5	0.0001	0.0001	TESS S59	
	2459927.33013	8771.5	0.0042	8771.5	-0.0002	0.0002	TESS S59	
	2459927.57604	8772.5	0.0044	8772.5	0	0.0002	TESS S59	
	2459927.69911	8773	0.0046	8773	0.0002	0.0002	TESS S59	
	2459927.82151	8773.5	0.0042	8773.5	-0.0002	0.0001	TESS S59	
	2459927.94495	8774	0.0048	8774	0.0004	0.0001	TESS S59	

Table 2. Continued

Target	BJD	Epoch(1)	O-C (1)	Epoch(2)	O-C (2)	Error	Source*	Filter
	2459928.06736	8774.5	0.0044	8774.5	0	0.0001	TESS S59	
	2459928.19050	8775	0.0047	8775	0.0003	0.0002	TESS S59	
	2459928.31330	8775.5	0.0046	8775.5	0.0002	0.0001	TESS S59	
	2459928.43635	8776	0.0048	8776	0.0004	0.0001	TESS S59	
	2459928.55879	8776.5	0.0044	8776.5	0	0.0002	TESS S59	
	2459929.54126	8780.5	0.0042	8780.5	-0.0002	0.0001	TESS S59	
	2459929.91031	8782	0.0048	8782	0.0004	0.0001	TESS S59	
	2459930.15625	8783	0.005	8783	0.0006	0.0001	TESS S59	
	2459930.52406	8784.5	0.0043	8784.5	-0.0001	0.0001	TESS S59	
	2459931.26124	8787.5	0.0045	8787.5	0.0001	0.0001	TESS S59	
	2459931.63021	8789	0.0049	8789	0.0005	0.0001	TESS S59	
	2459931.75268	8789.5	0.0046	8789.5	0.0002	0.0001	TESS S59	
	2459931.87590	8790	0.0049	8790	0.0005	0.0001	TESS S59	
	2459931.99805	8790.5	0.0043	8790.5	-0.0001	0.0001	TESS S59	
	2459932.12117	8791	0.0045	8791	0.0001	0.0001	TESS S59	
	2459932.24396	8791.5	0.0045	8791.5	0.0001	0.0001	TESS S59	
	2459932.48935	8792.5	0.0042	8792.5	-0.0002	0.0001	TESS S59	
	2459932.73548	8793.5	0.0047	8793.5	0.0003	0.0002	TESS S59	
	2459933.10427	8795	0.0049	8795	0.0005	0.0001	TESS S59	
	2459933.22639	8795.5	0.0042	8795.5	-0.0002	0.0001	TESS S59	
	2459933.71768	8797.5	0.0042	8797.5	-0.0002	0.0001	TESS S59	
	2459933.84124	8798	0.0049	8798	0.0005	0.0001	TESS S59	
	2459933.96356	8798.5	0.0044	8798.5	0	0.0002	TESS S59	
	2459934.20946	8799.5	0.0046	8799.5	0.0002	0.0002	TESS S59	
	2459934.45493	8800.5	0.0044	8800.5	0	0.0001	TESS S59	
	2459934.57830	8801	0.0049	8801	0.0005	0.0001	TESS S59	
	2459934.70091	8801.5	0.0047	8801.5	0.0003	0.0001	TESS S59	
	2459934.94618	8802.5	0.0043	8802.5	-0.0001	0.0001	TESS S59	
	2459935.31515	8804	0.0047	8804	0.0003	0.0001	TESS S59	
	2459935.43750	8804.5	0.0043	8804.5	-0.0001	0.0001	TESS S59	
	2459935.80656	8806	0.0048	8806	0.0004	0.0001	TESS S59	
	2459935.92883	8806.5	0.0042	8806.5	-0.0002	0.0001	TESS S59	
	2459936.17462	8807.5	0.0043	8807.5	0	0.0000	TESS S59	
	2459936.79104	8810	0.0066	8810	0.0022	0.0109	ZTF r	
	2460152.98337	9690	0.0049	9690	0.0007	0.0125	ZTF r	
	2460286.13884	10232	0.0045	10232	0.0004	0.0002	TESS S73	
	2460286.26074	10232.5	0.0036	10232.5	-0.0005	0.0002	TESS S73	
	2460287.85862	10239	0.0046	10239	0.0005	0.0002	TESS S73	
	2460287.98078	10239.5	0.0039	10239.5	-0.0002	0.0002	TESS S73	
	2460288.10401	10240	0.0043	10240	0.0002	0.0002	TESS S73	
	2460288.71769	10242.5	0.0038	10242.5	-0.0003	0.0002	TESS S73	
	2460288.84144	10243	0.0047	10243	0.0006	0.0002	TESS S73	
	2460288.96149	10243.5	0.0019	10243.5	-0.0022	0.0001	TESS S73	
	2460289.45470	10245.5	0.0038	10245.5	-0.0003	0.0002	TESS S73	
	2460289.70049	10246.5	0.0039	10246.5	-0.0002	0.0002	TESS S73	
	2460290.43748	10249.5	0.0039	10249.5	-0.0003	0.0002	TESS S73	
	2460290.56099	10250	0.0045	10250	0.0004	0.0001	TESS S73	
	2460290.68321	10250.5	0.0039	10250.5	-0.0002	0.0002	TESS S73	
	2460290.92869	10251.5	0.0037	10251.5	-0.0004	0.0002	TESS S73	

Table 2. Continued

Target	BJD	Epoch(1)	O-C (1)	Epoch(2)	O-C (2)	Error	Source⋆	Filter
	2460291.05211	10252	0.0043	10252	0.0002	0.0002	TESS S73	
	2460291.17459	10252.5	0.0039	10252.5	-0.0002	0.0002	TESS S73	
	2460291.66567	10254.5	0.0037	10254.5	-0.0004	0.0002	TESS S73	
	2460292.64848	10258.5	0.0038	10258.5	-0.0003	0.0002	TESS S73	
	2460292.77196	10259	0.0044	10259	0.0003	0.0002	TESS S73	
	2460292.89436	10259.5	0.004	10259.5	-0.0001	0.0002	TESS S73	
	2460293.01759	10260	0.0044	10260	0.0003	0.0001	TESS S73	
	2460293.13987	10260.5	0.0038	10260.5	-0.0003	0.0002	TESS S73	
	2460293.50921	10262	0.0047	10262	0.0005	0.0001	TESS S73	
	2460294.12265	10264.5	0.0039	10264.5	-0.0002	0.0002	TESS S73	
	2460294.49180	10266	0.0045	10266	0.0004	0.0002	TESS S73	
	2460295.47464	10270	0.0047	10270	0.0006	0.0002	TESS S73	
	2460295.59673	10270.5	0.0039	10270.5	-0.0002	0.0001	TESS S73	
	2460295.72033	10271	0.0047	10271	0.0006	0.0001	TESS S73	
	2460295.96579	10272	0.0045	10272	0.0004	0.0001	TESS S73	
	2460296.08792	10272.5	0.0038	10272.5	-0.0003	0.0000	TESS S73	
	2460296.21169	10273	0.0047	10273	0.0006	0.0001	TESS S73	
	2460296.33381	10273.5	0.004	10273.5	-0.0001	0.0002	TESS S73	
	2460296.45727	10274	0.0046	10274	0.0005	0.0001	TESS S73	
	2460296.94826	10276	0.0043	10276	0.0001	0.0001	TESS S73	
	2460297.07186	10276.5	0.005	10276.5	0.0009	0.0001	TESS S73	
	2460297.19417	10277	0.0045	10277	0.0004	0.0001	TESS S73	
	2460297.31628	10277.5	0.0038	10277.5	-0.0003	0.0001	TESS S73	
	2460297.56206	10278.5	0.0039	10278.5	-0.0002	0.0002	TESS S73	
	2460297.80772	10279.5	0.0038	10279.5	-0.0003	0.0002	TESS S73	
	2460298.17689	10281	0.0045	10281	0.0004	0.0002	TESS S73	
	2460298.29929	10281.5	0.0041	10281.5	0	0.0002	TESS S73	
	2460298.42253	10282	0.0045	10282	0.0004	0.0002	TESS S73	
	2460298.54462	10282.5	0.0037	10282.5	-0.0004	0.0002	TESS S73	
	2460298.66813	10283	0.0044	10283	0.0003	0.0001	TESS S73	
	2460298.79051	10283.5	0.0039	10283.5	-0.0002	0.0001	TESS S73	
	2460306.40624	10314.5	0.0037	10314.5	-0.0004	0.0001	TESS S73	
	2460307.02119	10317	0.0045	10317	0.0004	0.0002	TESS S73	
	2460307.14318	10317.5	0.0037	10317.5	-0.0004	0.0002	TESS S73	
	2460307.38883	10318.5	0.0036	10318.5	-0.0005	0.0002	TESS S73	
	2460307.51232	10319	0.0043	10319	0.0002	0.0001	TESS S73	
	2460307.88014	10320.5	0.0036	10320.5	-0.0005	0.0002	TESS S73	
	2460308.00360	10321	0.0042	10321	0.0001	0.0001	TESS S73	
	2460308.37171	10322.5	0.0038	10322.5	-0.0003	0.0001	TESS S73	
	2460308.61733	10323.5	0.0038	10323.5	-0.0003	0.0002	TESS S73	
	2460308.74077	10324	0.0044	10324	0.0003	0.0001	TESS S73	
	2460308.98653	10325	0.0044	10325	0.0003	0.0001	TESS S73	
	2460309.09729	10325.5	-0.0076	10325.5	-0.0117	0.0008	TESS S73	
	2460309.23216	10326	0.0044	10326	0.0003	0.0001	TESS S73	
	2460309.35444	10326.5	0.0038	10326.5	-0.0003	0.0002	TESS S73	
	2460309.47782	10327	0.0044	10327	0.0003	0.0002	TESS S73	
	2460309.60002	10327.5	0.0037	10327.5	-0.0003	0.0002	TESS S73	
	2460309.84567	10328.5	0.0037	10328.5	-0.0004	0.0001	TESS S73	
	2460309.96896	10329	0.0042	10329	0.0001	0.0001	TESS S73	

Table 2. Continued

Target	BJD	Epoch(1)	O-C (1)	Epoch(2)	O-C (2)	Error	Source⋆	Filter
	2460310.33692	10330.5	0.0036	10330.5	-0.0005	0.0002	TESS S73	
	2460310.46055	10331	0.0044	10331	0.0003	0.0002	TESS S73	
	2460310.70793	10332	0.0061	10332	0.002	0.0002	TESS S73	
	2460310.82826	10332.5	0.0036	10332.5	-0.0005	0.0002	TESS S73	
	2460310.95319	10333	0.0057	10333	0.0016	0.0002	TESS S73	
	2460311.07341	10333.5	0.0031	10333.5	-0.001	0.0003	TESS S73	
	2460311.19744	10334	0.0043	10334	0.0002	0.0002	TESS S73	
	2460311.32000	10334.5	0.004	10334.5	-0.0001	0.0002	TESS S73	
	2460311.56463	10335.5	0.003	10335.5	-0.0011	0.0007	TESS S73	
	2460311.69118	10336	0.0067	10336	0.0026	0.0004	TESS S73	
	2460311.79702	10336.5	-0.0103	10336.5	-0.0144	0.0012	TESS S73	
	2460312.17864	10338	0.0028	10338	-0.0013	0.0005	TESS S73	
	2460312.30180	10338.5	0.0031	10338.5	-0.001	0.0004	TESS S73	

⋆ Reference sources listed in Col. (8):

Agerer, F., 2006, Information Bulletin on Variable Stars, 5731.
Agerer, F., 2009, Information Bulletin on Variable Stars, 5874.
Agerer, F., 2011, Information Bulletin on Variable Stars, 5959.
Agerer, F., 2015, Information Bulletin on Variable Stars, 6149.
Alton, K., 2019, JAAVSO 47, 265.
Blättler, E., & Diethelm, R., 2001, Information Bulletin on Variable Stars, 5192.
Blättler, E., 2001a, BBSAG Bull., 126.
Blättler, E., 2002, BBSAG Bull., 128.
Blättler, E., 2003, Information Bulletin on Variable Stars, 5438.
Blättler, E., 2004, Information Bulletin on Variable Stars, 5543.
Blättler, E., 2006, Information Bulletin on Variable Stars, 5713.
Blättler, E., 2007, Information Bulletin on Variable Stars, 5781.
Blättler, E., 2009, Information Bulletin on Variable Stars, 5871.
Blättler, E., 2010, Information Bulletin on Variable Stars, 5920.
Diethelm, R., 2010, Information Bulletin on Variable Stars, 5945.
Diethelm, R., 2011, Information Bulletin on Variable Stars, 5992.
Locher, K., 2002, BBSAG Bull., 127.
Locher, K., 2002a, BBSAG Bull., 128.
Locher, K., 2003, Information Bulletin on Variable Stars, 5438.
Locher, K., 2004, Information Bulletin on Variable Stars, 5543.
Locher, K., 2005, Open European Journal on Varaible Stars, 3.
Moschner, W., 2018, Information Bulletin on Variable Stars, 6244.
Moschner, W., & Frank, P., 2016, Information Bulletin on Variable Stars, 6157.
ASAS-SN - All-Sky Automated Survey for Supernovae, (Shappee et al., 2014, Jayasinghe et al., 2019).
SWASP - Super-Wide Angle Search for Planets, Butters et al. 2010.
TESS - Transiting Exoplanet Survey Satellite, Ricker et al. 2015.
VSX - The International Variable Star Index, Watson, A., Henden, A.A., Price. A., 2006, Society for Astronomical Sciences Annual Symposim, 26, 47.
ZTF - Zwicky Transient Facility , Chen et al. 2020.

Table 3. New ephemeris of the systems.

System	Epoch	Period	Quadratic coefficient
TIC 9625707	BJD 2452500.18086(55)	0.28779576(4)	$9.06(6)^{-12}$
TIC 23081489	BJD 2457329.06648(55)	0.58574249(13)	$3.07(4)^{-10}$
TIC 426271738	BJD 2457772.39385(3)	0.24567480 (4)	$-2.68(7)^{-11}$

Table 4. Parameters of the secular rates of change of periods.

System	dP/dt (day yr^{-1})	dM_1/dt ($M_\odot$ yr^{-1})	dM_2/dt ($M_\odot$ yr^{-1})	dq/dt (yr^{-1})	dP/dt AM (day yr^{-1})
TIC 9625707	2.30^{-8}	-2.79^{-8}		1.63^{-7}	-3.90^{-8}
TIC 23081489	3.83^{-7}		1.17^{-7}	-8.02^{-8}	-1.81^{-7}
TIC 426271738	-7.98^{-8}		-1.48^{-7}	-7.47^{-7}	-2.90^{-8}

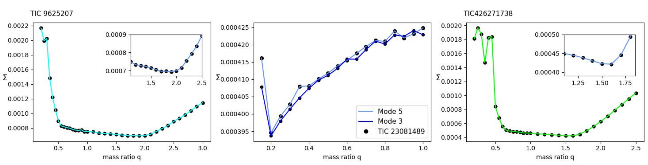

Figure 3. Dependence of the mean residual (Σ) on the mass ratio (q) for each system. The minimum Σ value for each system indicates the optimal mass ratio.

therefore, the final analysis for this system was restricted to `Modes` 3 and 5. The results of the q-search procedure for all systems are summarized in Figure 3, which shows the mean residual (Σ) of the fit plotted as a function of the mass ratio (q). The q value corresponding to the minimum Σ was then included among the adjustable parameters for a refined and detailed analysis.

The presence of third light (L_3) was negligible or undetectable in all systems analyzed. Except for TIC 23081489, the light curves of the other two systems exhibit the well-known O'Connell effect (O'Connell, 1951), characterized by the unequal heights of the primary and/or secondary maxima. This asymmetry is commonly attributed to the presence of hot or cool spots on one or both of the stellar components. Consequently, the following spot parameters were introduced as free parameters in the model: co-latitude (θ), longitude (ϕ), angular radius (γ), and temperature factor T_s/T_*. The results of our analysis are presented in Table 5, and the fits to the observational data are shown in Figure 4. The graphic representations of the systems are shown in Figure 5, which were generated using PyWD2015 (Güzel & Özdarcan, 2020).

6. ABSOLUTE ELEMENTS ESTIMATION

The estimation of absolute parameters is essential for comprehensively understanding the physical and dynamical properties of contact binary systems. For the systems under study, the absolute elements were derived using the empirical period-semimajor axis ($P - a$) relation first presented by Li et al. (2022) and updated by Poro et al. (2024), based on a sample of 414 contact binaries with orbital periods shorter than 0.7 d, Equation 5.

$$a = \left(0.372^{+0.113}_{-0.114}\right) + \left(5.914^{+0.272}_{-0.298}\right) \times P \quad (5)$$

Using the mass ratio (q) obtained from the light-curve solutions and Kepler's third law, the masses of the individual components were calculated as follows:

$$\frac{a^3}{G\,(M_1 + M_2)} = \frac{P^2}{4\pi^2}. \quad (6)$$

where $M_2 = qM_1$.

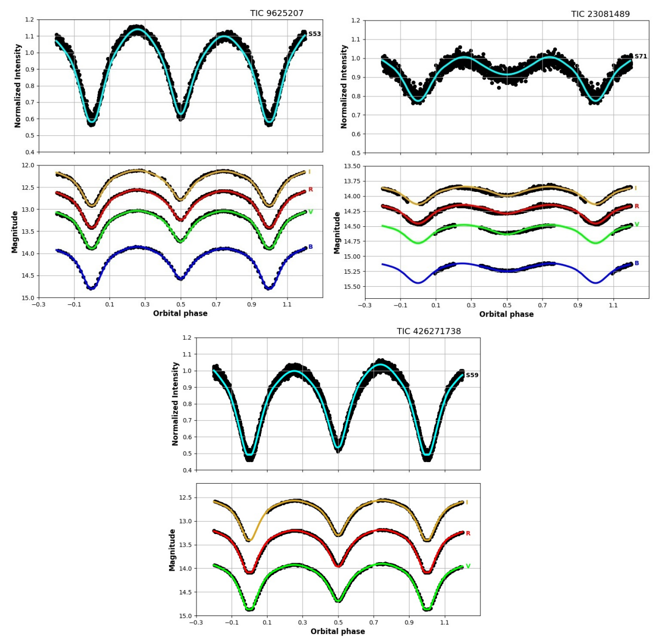

Figure 4. The continuous colored lines are the fit of the data points, upper panels for TESS and lower panels for SPM data.

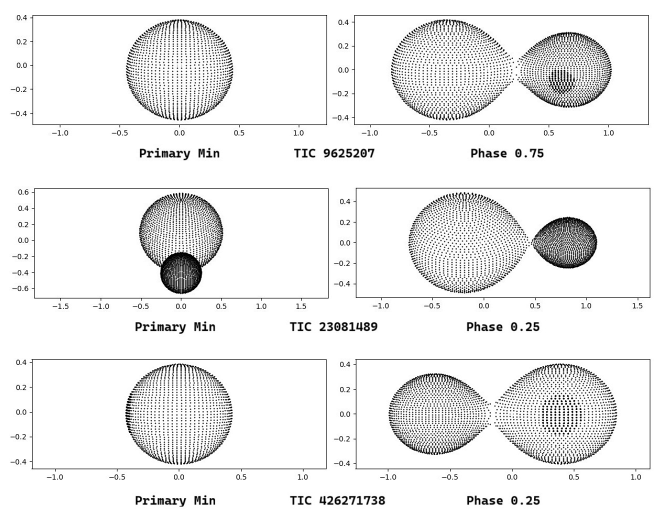

Figure 5. Graphical representations of the systems according to our solution.

The mean fractional radii ($r_{1,2}$) derived from the light-curve analysis were used to compute the stellar radii as follows: $R_{1,2} = ar_{1,2}$

The luminosities of the components were estimated using the Stefan-Boltzmann relation. Following Torres (2010), who adopted

Table 5. Parameter obtained from the Wilson-Devinney analysis.

Parameter	TIC 9625207	TIC 23081489	TIC 426271738
Period	0.28779576	0.58574249	0.24567480
Spectral type	G9 + K2	F1 + K4	K4-5 + K6
Subtype	W	A	W
i	83°.978±0°.423	69°.147±0°.393	87°.647±0°.303
T_1 *	5398 K	6970 K	4500 K
T_2	5029 K±9	4730 K±40	4258 K±4
$\Omega_{1,2}$	5.0299±0.0213	2.3054±0.0145	4.6171±0.0095
mass ratio	1.9048±0.0119	0.2301±0.0060	1.6076±0.0061
1/mass ratio	0.5249	-	0.6220
ΔT	369 K	2240 K	242 K
Fill-out	14.60%	0.37%	11.78%
X_{1B} *	0.657	-	-
X_{1V} *	0.374	-	0.766
X_{1R} *	0.249	−0.017	0.543
X_{1I} *	0.152	−0.076	0.352
X_{2B} *	0.204	-	-
X_{2V} *	0.443	-	0.044
X_{2R} *	0.507	0.712	0.236
X_{2I} *	0.522	0.684	0.356
L_{1B}	0.4523±0.0034	-	-
L_{1V}	0.4243±0.0026	-	0.4659±0.0020
L_{1R}	0.4053±0.0021	0.9089±0.0027	0.4307± 0.0016
L_{1I}	0.3958±0.0017	0.8941±0.0029	0.40930.0013
L_{1TESS}	0.3989±0.0041	0.9034±0.020	0.4103±0.0013
L_{2B}	0.5016±0.0041	-	-
L_{2V}	0.5214±0.0040	-	0.4751±0.0011
L_{2R}	0.5407±0.0038	0.0554±0.0010	0.5112±0.0009
L_{2I}	0.5557±0.0031	0.0709±0.0012	0.5336±0.0009
L_{2Tess}	0.5549±0.0035	0.0690±0.0010	0.5221± 0.0011
L_3	0	0	0
R_{1pole}	0.3114±0.0011	0.4767±0.0020	0.3239±0.0005
R_{1side}	0.3263±0.0013	0.5162±0.0027	0.3396±0.0006
R_{1back}	0.3639±0.0019	0.5398±0.0026	0.3759±0.0008
R_{2pole}	0.4176±0.0024	0.2435±0.0097	0.4031±0.0012
R_{2side}	0.4447±0.0031	0.2535±0.0116	0.4279±0.0016
R_{2back}	0.4760±0.0044	0.2870±0.0212	0.4601±0.0024
Lat spot	10°.3	-	88°.5
Long spot	80°.6	-	91°
Radius	18°.3	-	20°.2
T/F	1.09	-	1.05
Component	2	-	1
Mean residual (Σ)	0.00069381	0.00039312	0.00042109

Note:* Fixed parameters

Table 6. Estimated absolute elements.

System	TIC 9625207	TIC 23081489	TIC 426271738
$M_1(M_\odot)$	0.497±0.002	1.794±0.050	0.518±0.003
$M_2(M_\odot)$	0.947±0.005	0.413±0.020	0.833±0.003
$R_1(R_\odot)$	0.692±0.003	1.960±0.015	0.632±0.001
$R_2(R_\odot)$	0.952±0.007	1.002±0.010	0.785±0.002
$L_1(L_\odot)$	0.367±0.004	8.168±0.200	0.148±0.006
$L_2(L_\odot)$	0.493±0.009	0.453±0.020	0.183±0.001
$a(R_\odot)$	2.074±0.003	3.836±0.002	1.825±0.003
$log(g_1)(cgs)$	4.454±0.03	4.107±0.020	4.550±0.003
$log(g_2)(cgs)$	4.482±0.03	4.052±0.010	4.568±0.004
$M_{bol1}(mag)$	5.82±0.01	2.45±0.10	6.81±0.04
$M_{bol2}(mag)$	5.50±0.02	5.59±0.20	6.58±0.07
$logJ_0(cgs)$	51.53	51.77	51.48
$\mathcal{F}$	0.007	−0.028	0.001

the Sun's absolute bolometric magnitude as 4.73 mag, the absolute bolometric magnitudes of both components were calculated from the estimated luminosities via:

$$M_{\rm bol} - M_{\rm bol,\odot} = -2.5\log\left(L/L_\odot\right) \tag{7}$$

With masses and radii, the surface gravities (g) were computed on a logarithmic scale as follows:

$$g = G_\odot\left(M/R^2\right) \tag{8}$$

The orbital angular momentum (OAM, J_0) was evaluated according to Eker et al. (2006):

$$J_0 = \frac{q}{(1+q)^2}\sqrt[3]{\frac{G^2}{2\pi}M^5P} \tag{9}$$

Using the absolute elements listed in Table 6, the dynamical evolution of these contact binaries can be further investigated via their orbital angular momentum J_0 as described by Eker et al. (2006). Figure 6 presents the locations of our systems in the $logJ_0 - log$ $M_{\odot(tot)}$ plane. The curved borderline in the diagram separates the detached binaries from the contact systems. All three systems lie below the J_{lim} boundary, placing them unequivocally within the well-defined region of contact binaries, thus confirming their geometrical Roche lobe contact configurations. The derived absolute parameters are summarized in Table 6, which also includes the Flannery stability parameter (Flannery, 1976) ($\mathcal{F}$). This parameter highlights the system's response to mass transfer between the two components: a positive value indicates that the system can reach a stable configuration after mass exchange, whereas a negative value suggests a tendency toward dynamic instability.

6.1. Parameter of the progenitors of the systems and Darwin instability.

As demonstrated by Yildiz & Doğan (2013), the initial masses of the two components in contact binaries play crucial roles in their evolutionary paths. Following their method, we computed the initial masses of both components using the following equations:

$$M_{2i} = M_2 + \Delta M = M_2 + 2.50(M_L - M_2 - 0.07)^{0.64} \tag{10}$$

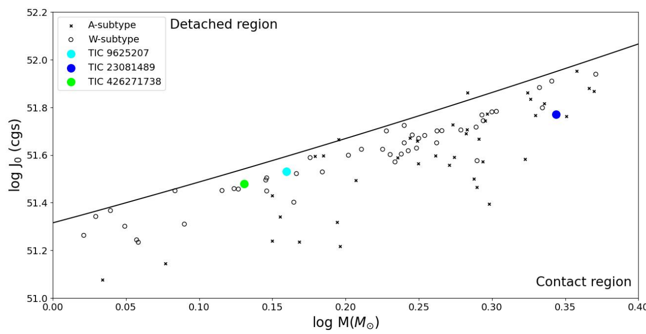

Figure 6. It shows three systems positioned beneath the J_{lim} curve, supporting their contact nature.

where M_{2i} is the initial mass of the secondary, M_2 is the current secondary mass, and M_L is the mass inferred from the mass-luminosity relation, defined as

$$M_L = 1.49M^{4.216}, \tag{11}$$

The initial mass of the primary component was computed as follows:

$$M_1 - M_{1i} = \Delta M - M_{lost} = \Delta M(1-\gamma). \tag{12}$$

where M_{1i} is the initial primary mass, M_1 is the present primary mass, M_{lost} is the total mass lost by the system, and γ is the ratio of M_{lost} to ΔM, for which we adopted the mean value $\gamma = 0.664$, as determined by Yildiz & Doğan (2013).

Hut (1980) investigated the stability of contact systems, showing that when the ratio of spin angular momentum to orbital angular momentum exceeds one-third, $\frac{J_{\rm spin}}{J_{\rm orb}} > \frac{1}{3}$, the system becomes dynamically unstable. Yang & Qian (2015) proposed the following formula to calculate this ratio:

$$\frac{J_{\rm spin}}{J_{\rm orb}} = \frac{q}{1+q}\left[(k_1r_1)^2 + (k_2r_2)^2\,q\right]. \tag{13}$$

where r_1 and r_2 are the relative radii of the primary and secondary components, respectively, and the dimensionless gyration radii are $k_1^2 = k_2^2 = 0.06$ (Li & Zhang, 2006). The computed progenitor parameters and stability criteria for our sample are listed in Table 7.

Table 7. Parameter of the progenitors of the systems and stability degree.

System	$1/q$	Subtype	M_{1i} $(M_\odot)$	M_{2i} $(M_\odot)$	M_{lost} $(M_\odot)$	J_{spin}/J_{orb}
TIC 9625207	0.524	W	0.70	1.24	0.49	0.059
TIC 426271738	0.622	W	0.76	0.72	0.14	0.050
System	q	Subtype	M_{1i} $(M_\odot)$	M_{2i} $(M_\odot)$	M_{lost} $(M_\odot)$	J_{spin}/J_{orb}
TIC 23081489	0.23007	A	1.43	1.50	0.72	0.033

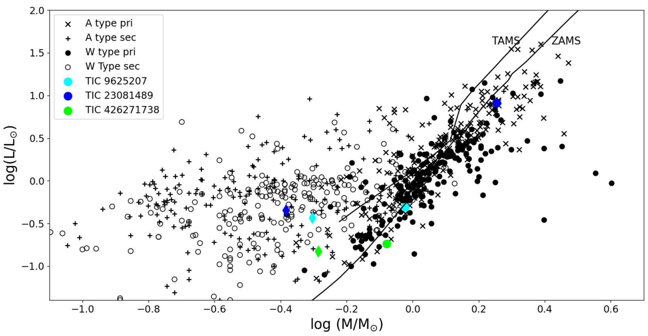

Figure 7. The positions of the system components on the log M - log L diagram is illustrated, where primaries are indicated by circles and secondaries by diamonds. The comparative sample of W UMa systems is taken from Latković et al. (2021), while the ZAMS and TAMS curves adopt solar chemical composition models from Girardi et al. (2000).

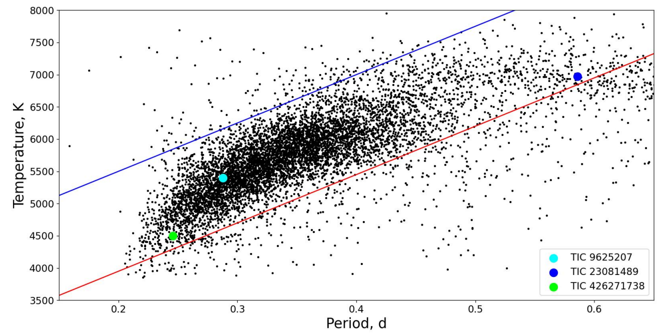

Figure 8. Correlation between orbital period and temperature based on parameters of 8510 contact binaries from Qian et al. (2020). The red and blue lines are the boundaries of normal EWs.

Given that all values of $\frac{J_{\rm spin}}{J_{\rm orb}}$ are less than 1/3, we conclude that all six systems are dynamically stable.

In the logarithmic mass-luminosity diagram shown in Figure 7, our three systems are plotted alongside other W- and A-type W UMa binaries compiled by Latković et al. (2021), as well as the Zero Age Main Sequence (ZAMS) and Terminal Age Main Sequence (TAMS) tracks computed by Girardi et al. (2000) for solar metallicity. It is evident from the figure that the components of our systems are in good agreement with the general distribution of well-studied W UMa binaries in the literature. The primary components lie close to the ZAMS line, occupying the region associated with the unevolved primaries of comparable systems. In contrast, the secondary components deviate markedly from the main sequence, similar to most secondaries in our sample, reflecting advanced evolutionary stages influenced by mass transfer.

The period-temperature relation for contact binaries was recently studied by Qian et al. (2020) using stellar atmospheric parameters from LAMOST. Their empirical diagram, reproduced here as Figure 8, delineates the boundaries for typical EW-type systems, with the red and blue lines marking the zones that segment the evolutionary stages of contact binaries. Systems near the red boundary tend to have longer orbital periods for a given temperature and generally exhibit marginal or shallow contact, with fill-out factors below 20%. These are interpreted as newly formed contact binaries at the onset of contact evolution. As their orbital periods decrease, they evolve toward marginal contact and shift toward the blue boundary, which represents deep-contact systems. Stars located between these boundaries constitute the population of normal contact EW systems. Our three systems fall within the boundaries of normal EW binaries, albeit with different positions. TIC 9625207, with orbital periods of approximately 0.27 d and mass ratios of 0.52, resides in the zone of normal contact binaries. Conversely, TIC 23081489 and TIC 426271738 were found closer to the red borderline, consistent with their status as newly formed contact binaries.

7. COMMENTS ON THE SYSTEMS - Common properties

From Table 5, it is evident that two of the three systems studied (except TIC 23081489) share more common physical properties than unique ones. Both exhibit total eclipses with orbital inclinations greater than 80° (Figure 5 and Table 5).

Terrell & Wilson (2005), Hambálek & Pribulla (2013), and Senavcı et al. (2016) emphasized the critical role of accurate light curve modeling in determining the geometric and physical parameters of eclipsing binaries. They highlight the necessity of high-precision photometry and sophisticated modeling methods, such as the Wilson-Devinney code, to accurately extract key parameters, such as inclination, stellar radii, and temperatures, especially for systems with total eclipses. Total eclipses impose strong constraints on stellar relative sizes and orbital inclination, as the eclipse duration and morphology are highly sensitive to these parameters. Spots were detected in both systems on the secondary component of TIC 9625207 and the primary component of TIC 426271738. They were slightly visible at shorter wavelengths but were absent at longer wavelengths. In the case of the TESS data, the asymmetry was more pronounced. The orbital periods of these two systems range from 0.245 to 0.287 days, shorter than the period peak near 0.30 - 0.31 days reported for W UMa-type binaries by Qian et al. (2020) and Latković et al. (2021). This suggests that our targets are typical W UMa-type contact binaries near the short-period limit. The "period limit" or "period cut-off" in eclipsing binaries was initially proposed by

Table 8. Comparison of the results obtained.

Parameter	TIC 9625207 This paper		TIC 9625207 Wang et al. (2024)
i	83.978°		83.47°
T_2/T_1	0.932		0.971
$1/q$	0.5249	q	0.59
fill-out	14.6%		2%
goodness of fit			0.886

Rucinski (1992) at 0.22 d marks the critical orbital period below which the binary properties change significantly. Recent studies utilizing extensive samples of eclipsing binaries discovered by space missions have revised this limit to approximately 0.15 d (Zhang & Qian, 2020); (Qian et al., 2020), though the validity of the 0.22-d cutoff remains debated (Li et al., 2019). According to the period-color relation for contact binaries, systems near the period cutoff are expected to consist of two K-type or later spectral type stars, indicating relatively cool components (Zhu et al., 2015). This constitutes the second shared characteristic of our systems. Most K-type contact binaries tend to be shallow W-subtype systems that exhibit light curve asymmetries (Sarotsakulchai et al., 2021). Their component temperature differences are typically a few hundred Kelvin, with some exceptions exhibiting nearly equal temperatures (Liu et al., 2023). Such K-type contact systems provide key observational tests for the Thermal Relaxation Oscillation (TRO) theory, postulated by Lucy (1967); Flannery (1976); Robertson & Eggleton (1977), Yakut & Eggleton (2005) and Li et al. (2008). The TRO model explains the observed light curve variability and period changes in certain contact binaries as cyclic oscillations in thermal equilibrium caused by energy transfer between components. This process may drive evolution involving transitions between the contact, semi-detached, and contact phases. The relatively cool temperatures of K-type stars influence the efficiency of the TRO mechanism in these stars. Our sample systems demonstrated good thermal contact, with temperature differences (ΔT) between 224 K and 369 K, suggesting effective energy exchange that tends to equalize their surface temperatures despite differences in intrinsic luminosity or stellar size. Given their late spectral types and low fill-out factors (14.6–11.8 %), these systems likely underwent one or more TRO cycles and currently appear to be evolving toward deeper contact configurations than their present state. However, the available observational data remain insufficient to detect period changes that could clarify the evolution of mass ratios in these binaries. Evidence of hot starspots, which typically arise from the kinetic impact of mass transfer between the binary components, is observed in both systems under consideration (Lee et al., 2006).

Wang et al. (2024) recently presented a catalogue of parameters for over 19,000 Catalina Sky Survey (CSS) contact binaries, derived using a novel Neural Network-Hamilton Monte Carlo (NNHMC) method combined with the PHOEBE (PHysics Of Eclipsing BinariEs) modeling code (Prša et al., 2016). This approach relies on generating thousands of synthetic light curves for training, validation, and testing, improving the parameter estimation for large eclipsing binary samples. This investigation, published after the completion of our analysis and during the preparation of this article, includes one of our target systems and offers a valuable opportunity to assess the consistency of our results.

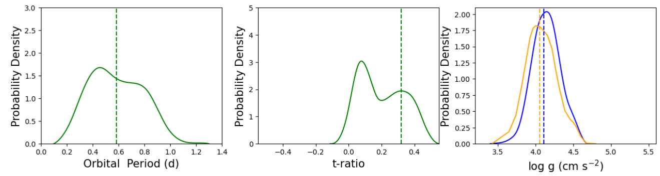

Figure 9. Probability density distributions of the orbital period (left), t-ratio (middle) and log g (right) of the nTCBs. The dashed lines represent TIC 23081489, in the third panel the blue and orange lines refer to the primary and secondary components respectively.

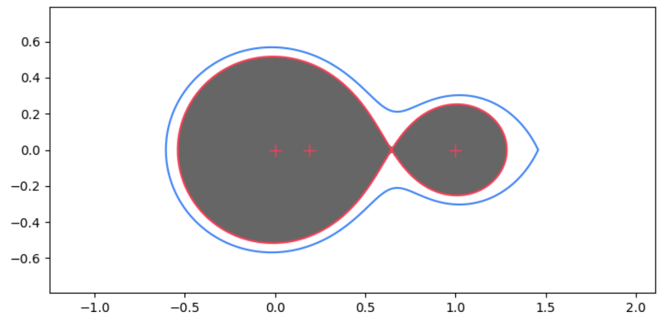

Figure 10. The configuration of the components of TIC 23081489 in the orbital plane is shown.

As summarized in Table 8, the discrepancies between the results of Wang et al. (2024) and ours are minor and encouraging. These differences likely arise because Wang et al. (2024) did not account for starspot effects (Aceves et al., 2025), while we detected a spot on one component of the system. Alternatively, these differences may stem from the distinct techniques employed by Wang et al. (2024) to derive the physical parameters (Panchal et al., 2025).

Our analysis of the remaining system, TIC 23081489, identified it as an A-subtype W UMa binary characterized by an unexpectedly low fill-out factor (f∼4%), a low mass ratio (∼0.2), and a substantial temperature difference between the components of approximately 2200 K. This solution is supported by the orbital period (∼0.58 d), the t-ratio, defined as

$$\text{t-ratio} = \frac{T_1 - T_2}{T_1} \tag{14}$$

and $\log g_{1,2}$ values, all consistent with the properties of non-thermal equilibrium contact binaries (nTCBs) studied by Wang et al. (2022). This correspondence is illustrated in the probability density distribution plots presented in Figure 9, where the dashed lines indicate the parameter values for our system. The positive value of the thermal decoupling parameter DT=0.32 (Lipari & Sistero, 1988) corroborates the classification of TIC 23081489 as an A-subtype system. Its light curve resembles that of a β Lyrae-type variable, exhibiting markedly unequal eclipse depths owing to the significant temperature difference between the components.

For systems of this nature, Lucy & Wilson (1979) introduced the class of B-type contact binaries: systems in or near geometric contact but far from thermal contact, characterized by large temperature differences between their components. Our results, that this low mass-ratio (∼ 0.23) system can only be modeled with a large temperature difference (ΔT > 2000 K) and a shallow contact degree f = 0.37% (Figure 10), may indicate that TIC 23081489 is at a critical evolutionary stage predicted by the Thermal Relaxation Oscillation (TRO) theory and suggest that it is a newly formed contact binary. It is plausible that TIC 23081489 is approaching the end of its semi-detached phase, during which it would exhibit an EB-type light curve, and has recently entered a shallow contact phase while maintaining a large temperature disparity. The apparent increase in the orbital period of TIC 23081489 Figure 2 warrants further confirmation through future observations.

This work is based on observations carried out at the Observatorio Astronómico Nacional on the Sierra San Pedro Mártir (OAN-SPM), Baja California, México. This research used the International Variable Star Index (VSX), a database operated at AAVSO, Cambridge, Massachusetts, USA. This research made use of the VizieR catalogue access tool, CDS, Strasbourg, France (DOI: 10.26093/cds/vizier). The original description of the VizieR service was published in 2000, A&AS 143, 23. This work used data from the European Space Agency (ESA) mission GAIA, processed by the Gaia Data Processing and Analysis Consortium (DPAC). Funding for the DPAC was provided by national institutions, particularly those participating in the Gaia Multilateral Agreement. This research also made use of the SIMBAD database, operated at CDS, Strasbourg, France, NASA Astrophysics Data System Abstract Service. This paper includes data collected by the TESS mission, which are publicly available from the Mikulski Archive for Space Telescopes (MAST). Funding for the TESS mission is provided by NASA's Science Mission Directorate. The authors gratefully acknowledge Dr. Orkun Özdarcan for his assistance with the PyWD2015 software. We would like to thank the anonymous referee for her/his useful comments, which have improved the quality of this paper. The authors would like to thank the AI language assistant provided by Perplexity AI for the support in English language revision.

REFERENCES

Aceves, H., Michel, R., Altamirano-Dévora, L., et al. 2025, RMxAA, 61, 49, doi: 10.22201/ia.01851101p.2025.61.01.04
Akerlof, C., Amrose, S., Balsano, R., et al. 2000, AJ, 119, 1901, doi: 10.1086/301321
Avdeeva, A. S., Kovaleva, D. A., Malkov, O. Y., & Zhao, G. 2024, MNRAS, 527, 7382, doi: 10.1093/mnras/stad3601
Binnendijk, L. 1965, Veroeffentlichungen der Remeis-Sternwarte zu Bamberg, 27, 36
—. 1970, VA, 12, 217, doi: 10.1016/0083-6656(70)90041-3
Bradstreet, D. H., & Guinan, E. F. 1994, in ASPC, Vol. 56, Interacting Binary Stars, ed. A. W. Shafter, 228
Butters, O. W., West, R. G., Anderson, D. R., et al. 2010, A&A, 520, L10, doi: 10.1051/0004-6361/201015655
Chen, X., Wang, S., Deng, L., et al. 2020, ApJS, 249, 18, doi: 10.3847/1538-4365/ab9cae
Claret, A., & Bloemen, S. 2011, A&A, 529, A75, doi: 10.1051/0004-6361/201116451
Claret, A., & Southworth, J. 2023, A&A, 674, A63, doi: 10.1051/0004-6361/202346478
Deeg, H. J. 2021, Galaxies, 9, doi: 10.3390/galaxies9010001
Drake, A. J., Graham, M. J., Djorgovski, S. G., et al. 2014, ApJS, 213, 9, doi: 10.1088/0067-0049/213/1/9
Eastman, J., Siverd, R., & Gaudi, B. S. 2010, PASP, 122, 935, doi: 10.1086/655938
Eggen, O. J., & Iben, Jr., I. 1989, AJ, 97, 431, doi: 10.1086/114993
Eker, Z., Demircan, O., Bilir, S., & Karataş, Y. 2006, MNRAS, 373, 1483, doi: 10.1111/j.1365-2966.2006.11073.x
Flannery, B. P. 1976, ApJ, 205, 217, doi: 10.1086/154266
Gaia Collaboration, Vallenari, A., Brown, A. G. A., et al. 2023, A&A, 674, A1, doi: 10.1051/0004-6361/202243940
Girardi, L., Bressan, A., Bertelli, G., & Chiosi, C. 2000, A&AS, 141, 371, doi: 10.1051/aas:2000126
Güzel, O., & Özdarcan, O. 2020, CoSka, 50, 535, doi: 10.31577/caosp.2020.50.2.535
Hambálek, Ľ., & Pribulla, T. 2013, CoSka, 43, 27
Hilditch, R. W. 2001, An Introduction to Close Binary Stars (Cambridge: MA, CUP)
Hut, P. 1980, A&A, 92, 167
Jayasinghe, T., Stanek, K. Z., Kochanek, C. S., et al. 2019, MNRAS, 486, 1907, doi: 10.1093/mnras/stz844
Kazarovets, E. V., Kireeva, N. N., Samus, N. N., & Durlevich, O. V. 2003, IBVS, 5422, 1
Kwee, K. K., & van Woerden, H. 1956, Bull. Astron. Inst. Netherlands, 12, 327
Latković, O., Čeki, A., & Lazarević, S. 2021, ApJS, 254, 10, doi: 10.3847/1538-4365/abeb23
Lee, J.-W., Lee, C.-U., Kim, C.-H., & Kang, Y.-W. 2006, JKAS, 39, 41, doi: 10.5303/JKAS.2006.39.2.041
Li, K., Gao, X., Liu, X.-Y., et al. 2022, AJ, 164, 202, doi: 10.3847/1538-3881/ac8ff2
Li, K., Kim, C.-H., Xia, Q.-Q., et al. 2020, AJ, 159, 189, doi: 10.3847/1538-3881/ab7cda
Li, K., Xia, Q.-Q., Michel, R., et al. 2019, MNRAS, 485, 4588, doi: 10.1093/mnras/stz715
Li, L., & Zhang, F. 2006, MNRAS, 369, 2001, doi: 10.1111/j.1365-2966.2006.10462.x
Li, L., Zhang, F., Han, Z., Jiang, D., & Jiang, T. 2008, MNRAS, 387, 97, doi: 10.1111/j.1365-2966.2008.12736.x
Li, X.-Z., Zhu, Q.-F., Ding, X., et al. 2024, ApJS, 271, 32, doi: 10.3847/1538-4365/ad226a
Liao, W. P., Qian, S. B., Soonthornthum, B., et al. 2017, PASP, 129, 124204, doi: 10.1088/1538-3873/aa8ded
Lipari, S. L., & Sistero, R. F. 1988, PASP, 100, 377, doi: 10.1086/132180
Liu, N. P., Qian, S. B., Liao, W. P., Huang, Y., & Yuan, Z. L. 2023, AJ, 165, 259, doi: 10.3847/1538-3881/acd04e
Lucy, L. B. 1967, ZAp, 65, 89
Lucy, L. B., & Wilson, R. E. 1979, ApJ, 231, 502, doi: 10.1086/157212
Luo, A. L., Zhao, Y. H., Zhao, G., & et al. 2019, VizieR Online Data Catalog: LAMOST DR5 catalogs (Luo+, 2019), VizieR On-line Data Catalog: V/164
O'Connell, D. J. K. 1951, Publications of the Riverview College Observatory, 2, 85
Paegert, M., Stassun, K. G., Collins, K. A., et al. 2021, arXiv e-prints, arXiv:2108.04778, doi: 10.48550/arXiv.2108.04778
Panchal, A., Joshi, Y. C., Joshi, V., & Chakraborty, A. 2025, ApJ, 986, 141, doi: 10.3847/1538-4357/add34d
Pecaut, M. J., & Mamajek, E. E. 2013, ApJS, 208, 9, doi: 10.1088/0067-0049/208/1/9
Poro, A., Tanriver, M., Michel, R., & Paki, E. 2024, PASP, 136, 024201, doi: 10.1088/1538-3873/ad1ed3
Prša, A., Conroy, K. E., Horvat, M., et al. 2016, ApJS, 227, 29, doi: 10.3847/1538-4365/227/2/29
Qian, S.-B., He, J.-J., Zhang, J., et al. 2017, RAA, 17, 087, doi: 10.1088/1674-4527/17/8/87
Qian, S.-B., Zhu, L.-Y., Liu, L., et al. 2020, RAA, 20, 163, doi: 10.1088/1674-4527/20/10/163

Ricker, G. R., Winn, J. N., Vanderspek, R., et al. 2015, JATIS, 1, 014003, doi: 10.1117/1.JATIS.1.1.014003

Robertson, J. A., & Eggleton, P. P. 1977, MNRAS, 179, 359, doi: 10.1093/mnras/179.3.359

Ruciński, S. M. 1973, AcA, 23, 79

Rucinski, S. M. 1992, AJ, 103, 960, doi: 10.1086/116118

Sarotsakulchai, T., Soonthornthum, B., Poshyachinda, S., et al. 2021, PASJ, 73, 1470, doi: 10.1093/pasj/psab090

Senavcı, H. V., Doğruel, M. B., Nelson, R. H., Yılmaz, M., & Selam, S. O. 2016, PASA, 33, e043, doi: 10.1017/pasa.2016.39

Serna, J., Hernandez, J., Kounkel, M., et al. 2021, ApJ, 923, 177, doi: 10.3847/1538-4357/ac300a

Shappee, B. J., Prieto, J. L., Grupe, D., et al. 2014, ApJ, 788, 48, doi: 10.1088/0004-637X/788/1/48

Smith, J. C., Stumpe, M. C., Van Cleve, J. E., et al. 2012, PASP, 124, 1000, doi: 10.1086/667697

Stępień, K. 2011, AcA, 61, 139, doi: 10.48550/arXiv.1105.2645

Stumpe, M. C., Smith, J. C., Catanzarite, J. H., et al. 2014, PASP, 126, 100, doi: 10.1086/674989

Terrell, D., & Wilson, R. E. 2005, Ap&SS, 296, 221, doi: 10.1007/s10509-005-4449-4

Torres, G. 2010, AJ, 140, 1158, doi: 10.1088/0004-6256/140/5/1158

Tylenda, R., Hajduk, M., Kamiński, T., et al. 2011, A&A, 528, A114, doi: 10.1051/0004-6361/201016221

Wang, J., Ding, X., Li, J., et al. 2024, ApJS, 273, 31, doi: 10.3847/1538-4365/ad5953

Wang, Z. H., Zhu, L. Y., & Yuan, K. 2022, MNRAS, 517, 1007, doi: 10.1093/mnras/stac2629

Wilson, R. E. 1990, ApJ, 356, 613, doi: 10.1086/168867

—. 1994, PASP, 106, 921, doi: 10.1086/133464

Wilson, R. E., & Devinney, E. J. 1971, ApJ, 166, 605, doi: 10.1086/150986

Yakut, K., & Eggleton, P. P. 2005, ApJ, 629, 1055, doi: 10.1086/431300

Yang, Y., & Liu, Q. 2003, A&A, 401, 631, doi: 10.1051/0004-6361:20030061

Yang, Y.-G., & Qian, S.-B. 2015, AJ, 150, 69, doi: 10.1088/0004-6256/150/3/69

Yildiz, M., & Doğan, T. 2013, MNRAS, 430, 2029, doi: 10.1093/mnras/stt028

Zhang, X.-D., & Qian, S.-B. 2020, MNRAS, 497, 3493, doi: 10.1093/mnras/staa2166

Zhu, L. Y., Qian, S. B., Jiang, L. Q., et al. 2015, in ASPC, Vol. 496, Living Together: Planets, Host Stars and Binaries, ed. S. M. Rucinski, G. Torres, & M. Zejda, 200

Zhu, L. Y., Zejda, M., Mikulášek, Z., et al. 2012, AJ, 144, 37, doi: 10.1088/0004-6256/144/2/37

Zhu, L.-Y., Zhao, E.-G., & Zhou, X. 2016, RAA, 16, 68, doi: 10.1088/1674-4527/16/4/068